Inelastic helium scattering studies of the vibrational spectroscopy and dynamics of ordered Ar, Kr, and Xe multilayers physisorbed on Ag(111)

K. D. Gibson and S. J. Sibener[a)]
Department of Chemistry and The James Franck Institute, The University of Chicago, Chicago, Illinois 60637

(Received 16 September 1987; accepted 7 December 1987)

This is the second of three papers discussing our studies of overlayers of Ar, Kr, and Xe physisorbed on Ag(111). All of these rare gases form ordered structures, which are azimuthally aligned but translationally incommensurate with the Ag substrate. In this paper, we discuss experiments in which we utilized the angle resolved time of flight of inelastically scattered 18 meV He atoms to examine the surface dynamics of multilayer rare gas films along the $\bar{\Gamma}$–$\bar{M}$ direction. This was done on a layer-by-layer basis for 2, 3, and ⩾20 layers for each of the rare gases. Unlike the monolayers, the vibrational modes observed for the multilayers show dispersion across the surface Brillouin zone, the amount of dispersion increasing with the number of adsorbed layers. These results reveal in detail how the surface dynamical properties of a thin film evolve towards those of a thick crystal as a function of increasing dimension. Lattice dynamics calculations, which utilize realistic gas phase pair potentials, reproduce the experimentally observed phonon dispersion relations quite well. We also examine the inelastic scattering probabilities and linewidths of the transitions. One of the more notable results is that the inelastic scattering probabilities vary by at most a factor of 2–3 across the entire surface Brillouin zone. Isothermal desorption measurements for the Xe overlayers are also discussed. Like the monolayer, the bilayer and trilayer exhibit nearly zeroth order desorption until ~90% of the top layer has desorbed, where the desorption kinetics become first order.

INTRODUCTION

In a previous paper (also referred to as paper I),[1] we discussed experiments which utilized the inelastic scattering of 18 meV He atoms to probe the surface dynamics of Ar, Kr, and Xe monolayers physisorbed on Ag(111). Isothermal desorption measurements were also presented for Xe monolayers. In this paper, we present similar results for ordered rare gas multilayer films, on a layer-by-layer basis, for 2, 3, and ⩾20 layers. The surface phonon dispersion relations for these systems reveal in fascinating detail how the surface dynamical properties of a thin film evolve towards those of a thick crystal with increasing overlayer dimension. Particular attention is focused on how the convergence proceeds as a function of phonon wave vector. Preliminary experimental results on this topic have been previously reported.[2–4] In a third paper of this series, we will present the results of our elastic He scattering measurements on monolayer and multilayer rare gas films. This paper (hereafter, paper III) includes experimental diffraction and selective adsorption measurements which are analyzed using quantum scattering calculations. The relative contributions of two-body and higher-order terms to the overall He–RG [RG = Ar, Kr, Xe] interaction potentials are examined in this work.

In recent years, inelastic He scattering has been used to study the surface dynamics of several materials. Of most interest to the present discussion is the work on adsorbate covered surfaces by Mason and Williams,[5–7] and Kern *et al.*[8,9] Mason and Williams examined rare gases physisorbed on several single crystal transition metal surfaces. The recent results of Kern *et al.* were for 1, 2, 3, and 25 layers of Kr and Xe physisorbed on Pt(111). The dynamical behavior exhibited by the Kr/Pt(111) and Xe/Pt(111) films was found in these studies to be quite similar to that reported in our previous work on Ag(111).[1–4] A further unifying feature for all of the above work on weakly physisorbed monolayer films is the presence of a nearly dispersionless surface vibrational mode. The characteristics of this Einstein mode were extensively discussed in paper I of this series.

Rare gas overlayers serve as excellent model systems because of the relative simplicity of the interactions involved. There is extensive information available, both experimental and theoretical, about the various potentials which are of concern here, including the He–RG [RG = Ar, Kr, Xe], RG–RG, and RG–Ag potentials. In addition, the structural and thermodynamic properties of these rare gases physisorbed on Ag(111) have been extensively studied by Webb and co-workers.[10–16] This large body of information provided an ideal starting point for our elastic and inelastic scattering experiments. In particular, these systems exhibit complete wetting, or type I, behavior, and were therefore a suitable choice for growing well ordered 1, 2, 3, and ⩾20 layer thin film structures. This allowed us to study how the surface properties of rare gas films evolve, on a layer-by-layer basis, as a function of increasing distance from the underlying substrate. The overlayer structures are all azimuthally aligned by translationally incommensurate with respect to the substrate lattice at all coverages and surface temperatures that were explored. That all three rare gases form incommensurate structures provides convincing proof that any registry forces arising from the slightly corru-

[a)] Alfred P. Sloan Fellow, 1984–1987.

gated Ag(111) substrate are very small. This allows the substrate, in many instances, to be accurately modeled as a smooth dielectric continuum.

The multilayer experiments presented in this paper are a logical continuation of our monolayer studies. Adatom–adatom and adatom–substrate interaction potentials do not change with increasing overlayer thickness. What does change is the surface–substrate distance, and, therefore, the environment of the surface adatoms. The evolution of the surface properties on a layer-by-layer basis gives basic insight into the contributions of the various components of the interaction potential to the overall charge density distributions at the surface. Furthermore, the sensitivity of the surface phonon modes to the presence of a buried interface depends critically on the wave vector of the mode in question. Long wavelength (small wave vector) excitations should obviously "feel" the influence of the underlying substrate at greater distances than short wavelength (large wave vector) excitations. Such differential sensitivity to the influence of a remote interface, as a function of phonon wave vector, is clearly revealed in these studies. This behavior should serve as a warning to those who ask how many layers it takes before the surface properties of a thin film reach those of a thick crystal—the answer depends on the characteristic length scale of the property in question.

He scattering was used in these studies as it is the ideal probe for examining the low energy phonon modes of these surfaces. It combines high surface sensitivity, sub-meV energy resolution, and sufficient momentum to probe the entire surface Brillouin zone (SBZ). The surface phonon dispersion relations were obtained by measuring the angle resolved time of flight (TOF) of inelastically scattered He. For all of the various reasons outlined in paper I, these experiments were performed with a relatively low energy 18 meV He beam. We also note that the inelastic scattering data were collected across the SBZ by varying the angle of the detector, while keeping the incident angle and beam energy fixed. This arrangement allows the inelastic scattering data to be compared with scattering calculations in a straightforward manner.

The organization of this paper is similar to paper I. The first section covers the experimental procedures. Section II discusses the isothermal desorption of Xe overlayers. Sections III and IV cover the energies of the inelastic transitions, and the inelastic scattering probabilities and linewidths.

EXPERIMENTAL

The experimental apparatus and procedures used have been described elsewhere.[1,17] So, in this section, only multilayer growth and those experimental methods peculiar to the multilayer rare gas systems will be covered.

The two most important requirements for growing a multilayer film were that a well-ordered monolayer be deposited, and that the Ag surface be clean, as determined by Auger spectroscopy. The issue of substrate cleanliness is crucial, as a small amount of adsorbed Cl can cause some of the monolayer domains to have an azimuthal alignment rotated by 30° with respect to the Ag substrate. When present in the monolayer, this misalignment persists when subsequent overlayers are deposited. The first step in growing a high quality multilayer film involved growing a well-ordered monolayer, using the dosing procedures described in paper I. Once it was determined that a good monolayer had been grown, by observing the intensities of the elastic diffraction features, the overlayers could be grown as described below for each rare gas. The desorption temperatures for the multilayers were not different enough for a procedure based solely on surface temperature to be used. Instead, the dosing time was controlled with a computer operated shutter. The exact dosing time for a single layer of gas to be deposited could be estimated by the dosing beam pressure, and rather precisely calibrated using temperature programmed thermal desorption (TPD), as described below. In all cases, the temperatures given are only approximate. Precise control of the temperature during growth was not found to be necessary. However, the best coherently diffracting overlayers were grown when dosing was done on a layer-by-layer basis.

For Xe, multilayer dosing was done on the prepared monolayer at $\Theta_i = 70°$ and a surface temperature $T_s = 46$ K. Once the bilayer was grown, the surface was annealed for 1 min at this temperature. If a trilayer was desired, the surface was dosed under the same conditions and annealed for a further minute. Finally, if many layers were desired, these were grown on the trilayer, dosing a layer at a time, with a 5 s annealing time between the deposition of each layer. The procedures for Kr and Ar were the same except for the surface tempertures used during dosing. For Kr, the surface temperature was 31 K, and for Ar, the surface temperature was 23 K.

As mentioned, dosing times were confirmed by TPD, an example of which is shown in Fig. 1 for trilayer Xe. The influence of the Ag–rare gas holding potential caused the monolayer to desorb at a much higher temperature than the overlayers, and so by comparing the total integrated area of the spectrum with that of the monolayer desorption peak, the coverage could be quantitatively determined.

It is important to note that for growing bilayers and

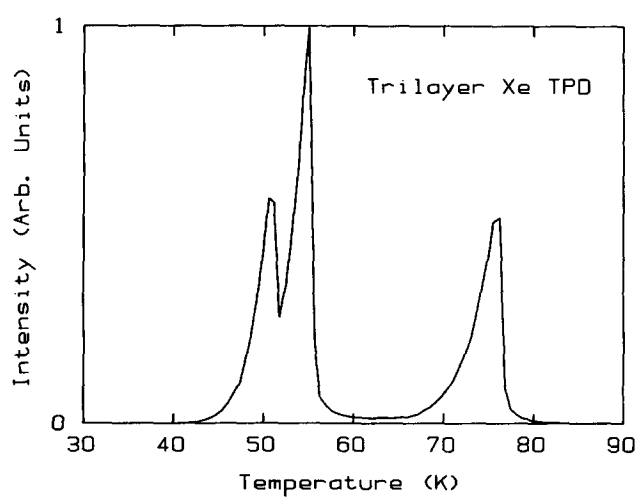

FIG. 1. A trilayer Xe TPD. The area of the monolayer desorption peak at $T_s \approx 75$ K yields a readily usable standard for calibrating multilayer coverages.

trilayers the dosing times for consecutive layers were equal. This implies that the sticking coefficients for a rare gas on a monolayer or bilayer are the same near their desorption temperatures. This dosing time was also the same as that required to grow a monolayer near its desorption temperature. As pointed out in paper I, it appeared that the sticking coefficient for the rare gases on the Ag substrate was nearly unity, and so the sticking coefficients for the rare gases on a monolayer or bilayer of the same gas must also be close to unity, even near the desorption temperature.

Besides confirming dosing times, TPD runs were also used to confirm the coverage after a series of experiments were done on a particular multilayer film. For the bilayers and trilayers, only the results for films that were within about 10% of the expected coverage were used. It is important to note that for growing thick films, small errors in dosing time accumulated, resulting in the growth of a nonintegral number of layers. The number of defects thus introduced depends upon whether or not the assumedly partial top layer aggregates into large islands.

Figures 2–4 show He diffraction spectra from Ar, Kr, and Xe multilayers, taken at $\Theta_i = 45°$ along the $\langle 11\bar{2} \rangle$ azimuth. It is important to note that the azimuthal alignment of the adlayers is the same as the Ag substrate, within 0.5°, in agreement with the results of Unguris *et al.*[10,12,15] That the overlayer structures are well ordered is shown by the presence of the elastic diffraction features, and by the relatively narrow angular spread of the elastic features. As in paper I, the coherence length of the surface was estimated to be on the order of 100 Å, comparable to that of the Ag substrate. This observation indicates that we are not growing roughened films, even for the case of the thick films, where there was a nonintegral number of layers. Table I gives the probabilities for the elastic scattering shown in Figs. 2–4. Discussion of elastic scattering will be given in paper III.[18] The positions of the elastic features also allow the surface lattice constants to be determined by using the conditions of energy

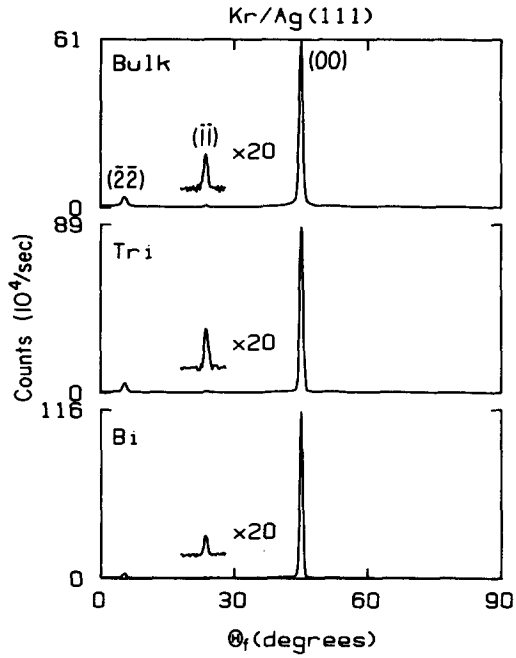

FIG. 3. Diffraction spectra for Kr multilayers along the $\langle 11\bar{2} \rangle$ azimuth, taken at $\Theta_i = 45°$ with an 18 meV He beam at a surface temperature of 22 K. Spectrum labeled bulk is 39 layers. Intensities are only roughly comparable, as the experimental conditions were not exactly the same. All kinematically allowed elastic features are observed.

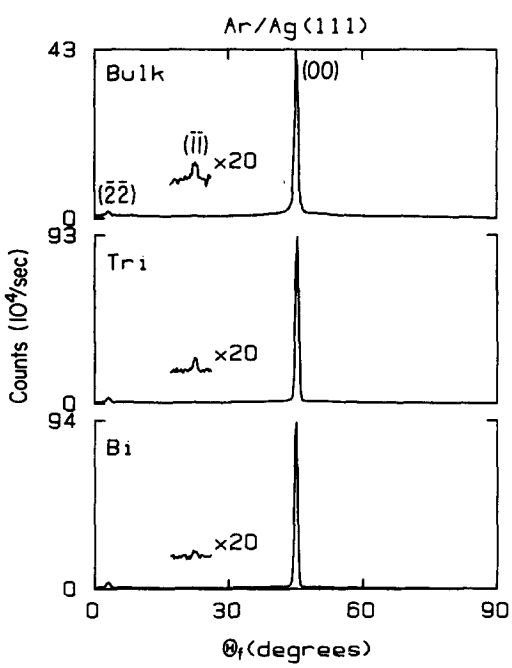

FIG. 2. Diffratction spectra for Ar multilayers along the $\langle 11\bar{2} \rangle$ azimuth, taken at $\Theta_i = 45°$ with an 18 meV He beam at a surface temperature of 21 K. Spectrum labeled bulk is 35 layers. Intensities are only roughly comparable, as the experimental conditions were not exactly the same. All kinematically allowed elastic features are observed.

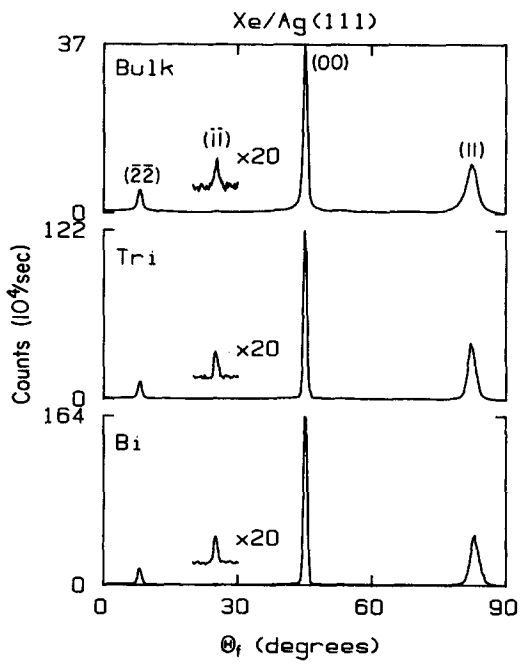

FIG. 4. Diffraction spectra for Xe multilayers along the $\langle 11\bar{2} \rangle$ azimuth, taken at $\Theta_i = 45°$ with an 18 meV He beam at a surface temperature of 22 K for the bilayer and trilayer, and 24 K for the spectrum labeled bulk, which is 25 layers. Intensities are only roughly comparable, as the experimental conditions were not exactly the same. All kinematically allowed elastic features are observed.

TABLE I. Elastic scattering probabilities (in %) for the diffraction spectra shown in Figs. 2–4. The first number is Debye–Waller corrected to 0 K (see the text), while the number in parentheses is the value at the temperature at which the data were taken.

	(11)	Ar (00)	$(\bar{1}\bar{1})$	$(\bar{2}\bar{2})$
Bilayer	···	2.78(1.24)	0.007(0.003)	0.141(0.051)
Trilayer	···	4.24(1.30)	0.022(0.005)	0.201(0.045)
35 layers	···	2.61(0.588)	0.022(0.004)	0.110(0.017)
	(11)	Kr (00)	$(\bar{1}\bar{1})$	$(\bar{2}\bar{2})$
Bilayer	···	4.58(1.65)	0.041(0.012)	0.191(0.053)
Trilayer	···	4.42(1.34)	0.076(0.019)	0.348(0.077)
39 layers	···	3.40(0.859)	0.051(0.010)	0.359(0.064)
	(11)	Xe (00)	$(\bar{1}\bar{1})$	$(\bar{2}\bar{2})$
Bilayer	1.82(1.10)	3.54(1.69)	0.032(0.013)	0.385(0.151)
Trilayer	2.07(1.12)	3.58(1.45)	0.037(0.013)	0.477(0.151)
25 layers	0.832(0.352)	1.84(0.514)	0.016(0.004)	0.376(0.075)

and crystal momentum conservation. Table II gives the surface lattice constants of the overlayers. Unlike the monolayer films, the overlayer lattice constants are the same as the bulk values from x-ray diffraction,[19] within the experimental error of our measurements. Also, these lattice constants are observed immediately after dosing, unlike the Xe monolayer, which slowly compresses by several thousandths of an Å over the period of a few hours.[1,13]

XE MULTILAYER DESORPTION

Figures 5 and 6 show examples of isothermal desorption spectra for the top layers of a Xe bilayer and trilayer, respectively, monitored at $\Theta_f = 0°$. Data were taken by pulse counting over discrete time intervals of constant width. The width of the sampling interval chosen depended on the surface temperature, and thus the rate of desorption. As was the case in paper I, due to the fact that the differentially pumped and highly collimated detector viewed only a small portion of the crystal, we did not have to worry about corrections due to pumping speed (the pressure rise in the detector was negligible), or signal from Xe desorbed off of the manipulator. A series of these experiments were performed for a range of temperatures for which the desorption could be monitored. For both the bilayer and trilayer, the general features for the desorption of the top layer were the same as that of the monolayer. The desorption rate was constant, or nearly so, until approximately 90% of the top layer had desorbed. At this point, the desorption rate began decreasing with decreasing coverage.

TABLE II. Values of the surface lattice constants (in Å). The column labeled many layers is for 25 or more layer films. Estimated error is ± 0.02 Å. The column labeled bulk is for the bulk x-ray values.

	Monolayer	Bilayer	Trilayer	Many layers	Bulk[a]
Ar(21 K)	3.79	3.77	3.77	3.77	3.76
Kr(22 K)	4.02	4.00	4.01	4.00	4.00
Xe(24 K)	4.38	4.34	4.34	4.33	4.34

[a] Reference 19.

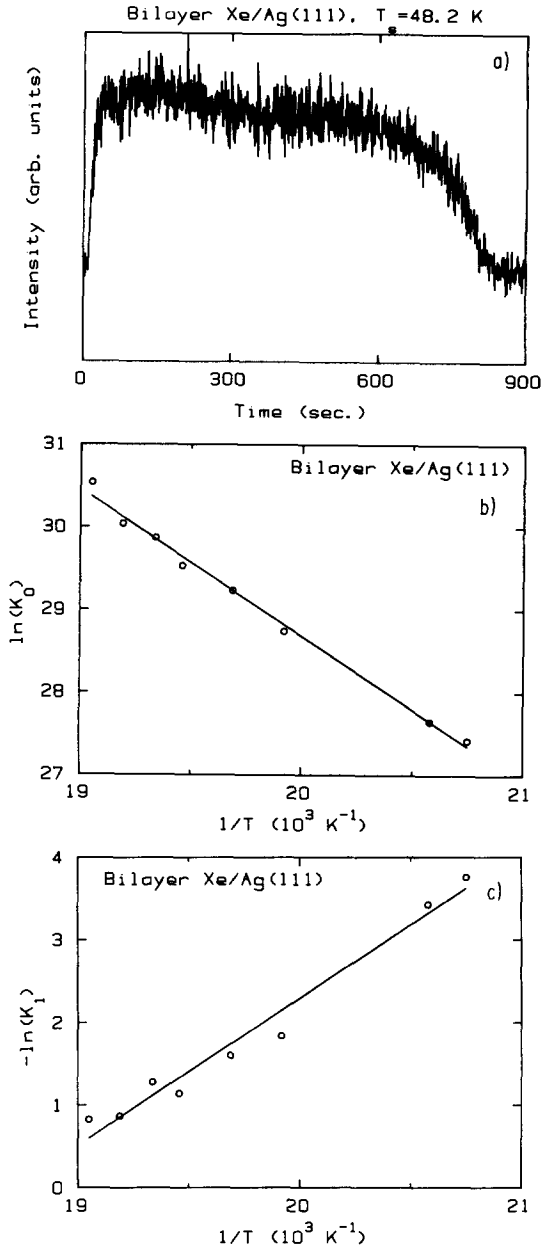

FIG. 5. (a) is an example of an isothermal desorption spectrum of the top layer of a Xe bilayer physisorbed on Ag(111). It shows the general features of all of the isothermal desorption spectra, the rate being nearly zeroth order until approximately 90% of the second layer has desorbed, where the desorption signal shows an exponential decrease, which is the first order regime. (b) is an Arrhenius plot for the zeroth order desorption, and (c) is an Arrhenius plot for the first order desorption.

We can write the desorption rate equation in the general form

$$-\frac{\partial\theta}{\partial t} = \theta^n k_n = \theta^n \nu_n \exp\left(\frac{-E_a}{RT}\right), \tag{1}$$

where θ is the coverage, n is the order of the desorption, k_n is the rate constant, ν_n is the frequency factor, and E_a is the activation energy for desorption. A plot of ln (k_n) vs $1/T$

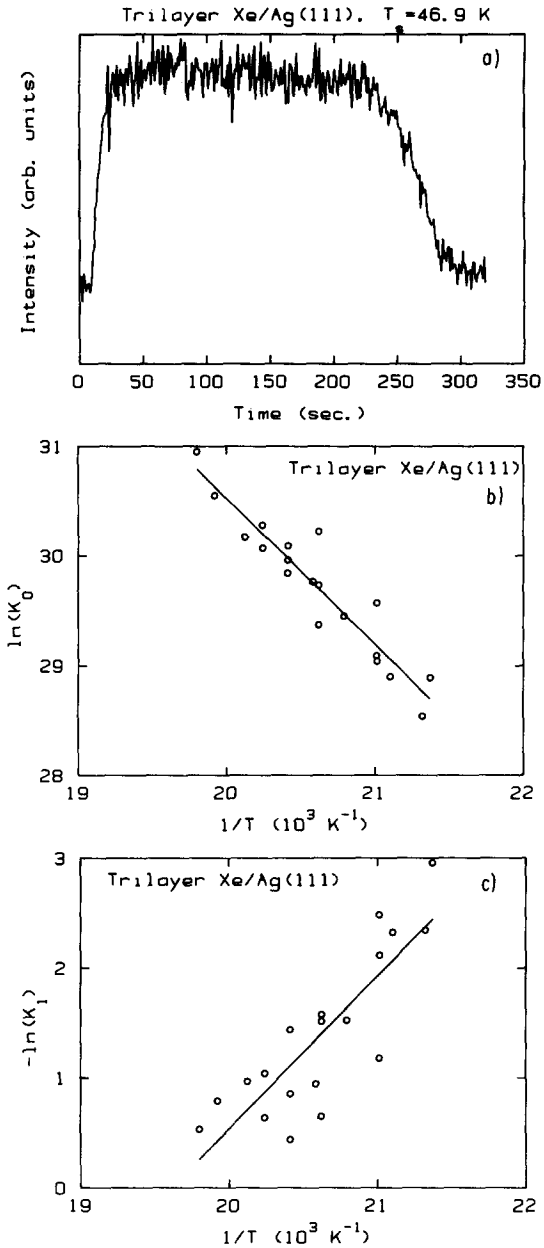

FIG. 6. (a) is an example of an isothermal desorption spectrum of the top layer of a Xe trilayer physisorbed on Ag(111). It shows the general features of all of the isothermal desorption spectra, the rate being nearly zeroth order until approximately 90% of the third layer has desorbed, where the desorption signal shows an exponential decrease, which is the first order regime. (b) is an Arrhenius plot for the zeroth order desorption, and (c) is an Arrhenius plot for the first order desorption.

should then be a straight line with slope $-E_a/R$ and intercept ν_n.

For the first part of the desorption, assuming zeroth order kinetics, the rate constant k_0 was determined from the relation

$$Ci_{\rm ms} = -\frac{\Delta\theta}{\Delta t} = k_0, \tag{2}$$

where $i_{\rm ms}$ is the mass spectrometer signal during the time interval Δt, and C is a proportionality constant. To determine C, it is only necessary to determine the total integrated value of $i_{\rm ms}$ for the desorption of a complete layer, and θ_0, the saturation coverage for a full Xe layer. Using a lattice constant of 4.34 Å, full coverage is $\theta_0 = 6.13\times10^{14}$ atoms/cm^2. Plots of $\ln(k_0)$ vs $1/T$ are shown in Figs. 5 and 6 for bilayer and trilayer Xe, respectively. The portion of each spectra with a decreasing desorption rate was fit with a single exponential, and the first order rate constant k_1 was determined using the relation

$$i_{\rm ms} = C' \exp[-k_1(t-t_1)], \tag{3}$$

where t is the time, t_1 is some time at which the desorption is first order, and C' is a constant of proportionality dependent on t_1 and the sampling rate. As in the case of the monolayer, this procedure gave a good fit to the data over approximately the last 70% of the region where the desorption rate is decreasing. Figures 5 and 6 show plots of $-\ln(k_1)$ vs $1/T$ for the first order desorption regime for the top layer of bilayer and trilayer Xe.

Table III gives the values of E_a and ν_n for both the zeroth and first order regions of 1, 2, and 3 layers of adsorbed Xe. The error bars represent the 95% confidence interval for the fits of $\ln(k)$ vs $1/T$. Accuracy is mainly determined by the systematic uncertainty in the temperature measurements. Assuming the temperature calibration is within 3 K, the value of ν_n is correct within an order of magnitude, and E_a is correct to within about 0.4 kcal/mol. However, the relative values should be nearly correct within the limits of precision given. Behm *et al.*[20] have also observed zeroth order desorption for monolayer and bilayer Xe physisorbed on Ag(111). Their values of E_a are 5.2 kcal/mol for the monolayer and 4.3 kcal/mol for the bilayer, which were determined using temperature-ramped (i.e., not isothermal) thermal desorption measurements. We cannot presently explain the discrepancy between our results and theirs, which is particularly large for the bilayer. However, we feel that isothermal measurements of desorption kinetics are a cleaner probe for these systems than are TPD line shapes.

TABLE III. Activation energies and frequency factors for the desorption of the top layer of monolayer, bilayer, and trilayer Xe/Ag(111) for the two different orders of desorption kinetics observed. The error bars represent the precision (see the text). Also listed are the latent heats of adsorption for monolayer and bilayer, and the latent heat of sublimation of the bulk.

	Zeroth order desorption E_a (kcal/mol)	ν_0(cm^2 s)$^{-1}$
Monolayer	4.77 ± 0.10	$(1.2\pm1.0)\times10^{28}$
Bilayer	3.53 ± 0.13	$(7\pm9)\times10^{27}$
Trilayer	2.65 ± 0.22	$(7\pm15)\times10^{24}$
	First order desorption E_a (kcal/mol)	ν_1(s^{-1})
Monolayer	4.95 ± 0.25	$(2\pm4)\times10^{15}$
Bilayer	3.53 ± 0.24	$(3\pm6)\times10^{14}$
Trilayer	2.76 ± 0.46	$(7\pm34)\times10^{11}$
	Latent heats (kcal/mol)	
Monolayer[a]	5.19	
Bilayer[a]	3.99	
Bulk[b]	3.71	

[a] Reference 11.
[b] Reference 24.

Opila and Gomer[21] also studied the thermal desorption of Xe physisorbed on a single crystal transition metal surface, in their case W(110). The general features of the Xe desorption they observed are qualitatively the same as our results, there being regions of zeroth and first order kinetics in the isothermal desorption spectra. One quantitative difference is that for the Xe/W(110) system, the zeroth to first order transition occurs at approximately 30% of a full layer. This may due to a higher defect density in their films. Since the Xe–surface holding potential for the two close-packed transition metal surfaces Ag(111) and W(110) are not equal, the values of E_a for monolayer desorption from the two surfaces are significantly different. For the bilayer and trilayer, the values of E_a are nearly the same for the two different substrates due to the decreasing importance of the surface–substrate holding potential with increasing surface–substrate distance. Another difference between our results and the Xe/W(110) system is that the values of ν_n are, in general, higher for Xe physisorbed on Ag(111).

The change from zeroth to first order desorption kinetics is indicative of a 2D order–disorder transition,[22] where the zeroth order kinetics occur when there is an equilibrium between ordered and disordered phases of the adatoms. That the desorption of the top layer of monolayer, bilayer, and trilayer is qualitatively similar suggests a common mechanism for the desorption. The quantitative differences are at least partially due to the Xe–substrate holding potential, and may also reflect some differences in the phonon–phonon interactions by which heat is transferred from the substrate through the adatoms to the outermost layer. In paper I, we discussed the desorption terms of mechanism 3b given in the paper by Opila and Gomer. This mechanism proposes an equilibrium between both a dense ordered phase and a more dilute random phase, plus equal desorption rates from each phase. The transition from zeroth to first order kinetics would then occur where the dense phase was depleted. A similar explanation for zero order desorption is given by Venables and Bienfait.[23] Here it is assumed that the dense phase only desorbs indirectly through two disordered phases, one disordered phase existing between islands of the dense phase, and the other existing on top of the islands. Both of these mechanisms require that the sticking coefficient be equal for the phases from which the desorption is taking place. As stated in paper I, it appeared that the sticking coefficient for the monolayer was about unity near the desorption temperature, and appeared to be nearly coverage independent. If there are desorbing phases, their relative proportion should be changing with increasing coverage, so the sticking coefficients must be nearly equal for each phase. Since growing a second or third layer near their desorption temperatures took the same amount of time as growing a monolayer, it would seem that their sticking coefficients are also nearly coverage independent. Thus, at the actual temperature of desorption, it does not seem unreasonable that the sticking coefficients for the desorbing phases are nearly the same. For both of these mechanisms, E_a should be the same for zeroth and first order desorption, which experimentally is the case, within the precision of our measurements.

Unlike the case of the monolayer, we were unable to look for diffraction from the desorbing layers during desorption, as the underlayers were diffracting also, and had nearly identical lattice constants. Consequently, we have no experimental measure of when ordered islands of the top layer are depleted.

The values of the latent heat of condensation of the monolayer and bilayer[13] and the latent heat of sublimation for the bulk,[24] which should be similar to that of the trilayer, are given in Table III. E_a is only slightly smaller than the enthalpy for the monolayer, $\sim$0.5 kcal/mol less than the enthalpy for the bilayer, but $\sim$1 kcal/mol less in the case of the trilayer. That E_a is less than the corresponding enthalpy was also observed by Opila and Gomer. That the activation energies can be smaller has been predicted by Efrima *et al.*[25] and Tully.[26] They attribute this behavior to dynamical effects. A simplified explanation is that once an adatom has reached some critical vibrational level, which is still below the continuum, the transition rate to the continuum is greater than the probability that the adatom will lose vibrational quanta. The measured value of E_a is then the energy needed to reach this critical vibrational level, rather than the energy needed to desorb the adatom. We have no explanation for the greater differences as the number of layers increase.

INELASTIC SCATTERING: TRANSITION ENERGIES

Figures 7, 8, and 9 show some TOF spectra for an 18 meV He beam scattering from 2, 3, and $\geqslant$20 layers of Ar, Kr, and Xe physisorbed on Ag(111), taken at $\Theta_i = 45°$. Data were taken with $\sim$1 h of signal averaging. Absolute scattering intensities were similar to those from the monolayers at the same incident angle. Since the scattering intensity was good at $\Theta_i = 45°$, most of the spectra were taken with this angle of incidence. The arrows indicate the position of the elastic channel. As was the case for the monolayers, a feature appears at this position in the off-specular TOF spectra. At final angles near the specular, there is a contribution to this peak due to the angular resolution of the apparatus. However, at other angles, this incoherent elastic feature is probably due to scattering from crystal defects. It shows up distinctly in the TOF spectra for the bilayers and trilayers. In the case of the thick films, it only shows up clearly for final angles where the scan curves allow interactions only with higher energy phonons. At other final angles, it generally appears as a shoulder on an inelastic feature. There are also at least two distinct inelastic features in most of the spectra, one on either side of the elastic feature. The one to the left corresponds to He scattered at final energies higher than the incident energy, and thus to phonon annihilation. The inelastic feature immediately to the right of the elastic channel, which generally was the most intense, is for inelastic transitions where the scattered He has lost energy, and a phonon has been created. For the purposes of mapping out the phonon dispersion relationships, final angles were chosen so as to follow this inelastic feature for parallel momentum transfers from $\bar{\Gamma}$ to $\bar{M}$ (the $\langle 11\bar{2}\rangle$ azimuth). On the phonon creation side, many of the spectra show one more distinct inelastic feature, and also a broad shoulder.

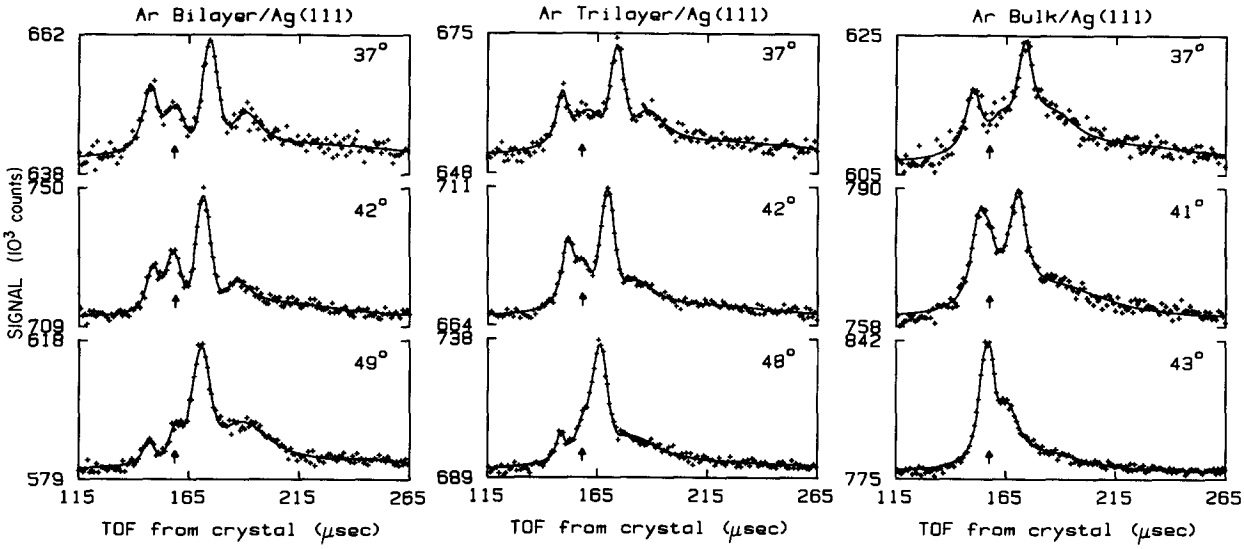

FIG. 7. TOF spectra for an 18 meV He beam scattering from Ar multilayers physisorbed on Ag(111), taken along the $\langle 11\bar{2}\rangle$ azimuth, with $\Theta_i = 45°$. T_s, the surface temperature, was ~21 K. For the spectra labeled bulk, the bottom two are ~34 layers, and the top one is ~50 layers. Crosses are the data points, and solid lines are the results for the least-squares fit. Numbers in the upper right-hand corner were the detector angles for each of the spectra.

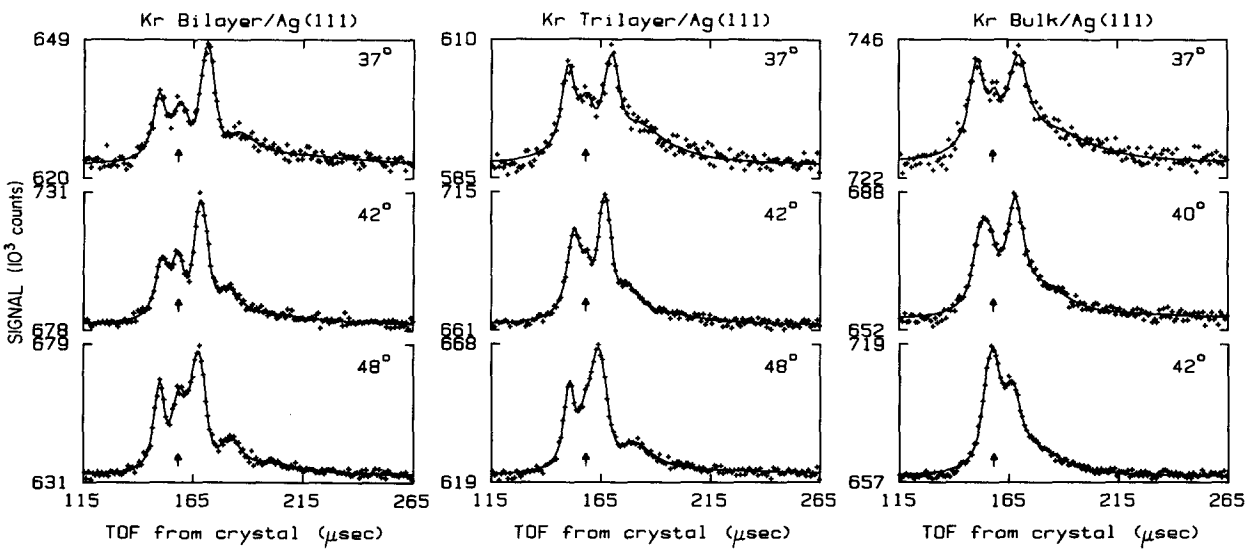

FIG. 8. The same as Fig. 7 for Kr multilayers, with $T_s = 22$ K. Spectra labeled bulk are between 28 and 30 layers.

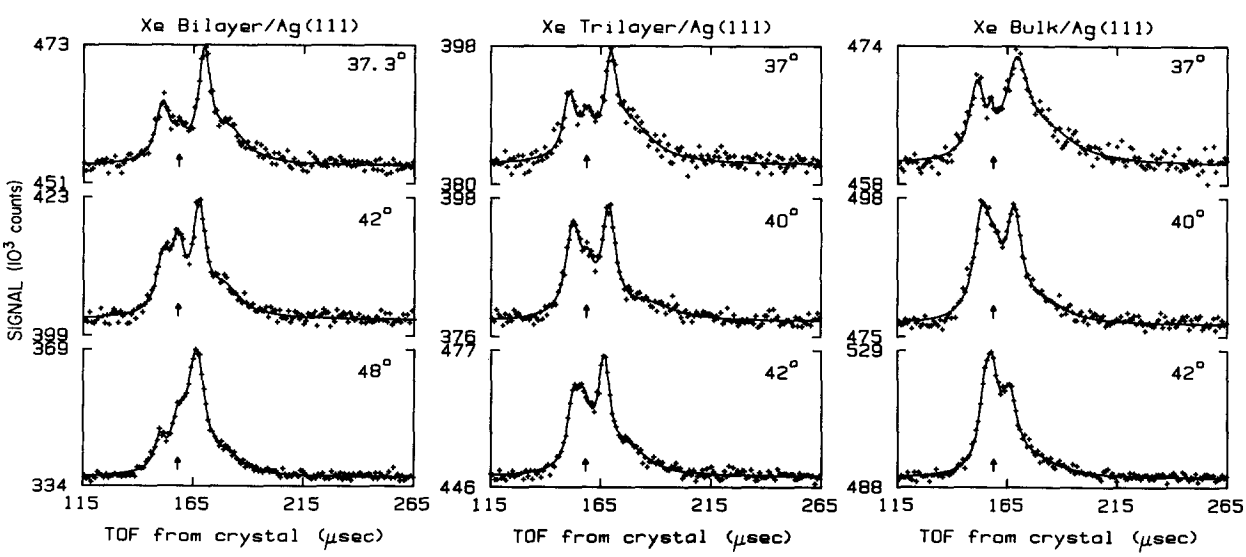

FIG. 9. The same as Fig. 7 for Xe multilayers, with $T_s = 24$ K. Spectra labeled bulk are between 20 and 22 layers.

The method used to analyze the data was presented in paper I, and so will only be briefly described here. The first step was to use a nonlinear least-squares routine to determine the time of flight for the maxima of the features in the spectra. The fitting function used was the sum of Lorentzian and Gaussian line shapes, but the precise line shape used for a particular feature was rather arbitrary, the main criterion being how well a spectrum was fit. The transition energies could then be determined by conservation of energy. For time-of-flight measurements, the resulting equation is

$$n\hbar\omega = E_f - E_i = \left(\frac{Mv_i^2}{2}\right)\left[\left(1+\frac{v_i\Delta t_{xd}}{l_{xd}}\right)^{-2} - 1\right], \quad (4)$$

where Δt_{xd} is the time shift for the inelastic feature, l_{xd} is the distance from crystal to detector, M is the He atom mass, and v_i is the velocity of the incident He atoms. With the final energy determined, the parallel momentum transfer is given by

$$Q = \left(\frac{2M}{\hbar^2}\right)^{1/2}\left[(\sqrt{E_f})\sin(\Theta_f) - (\sqrt{E_i})\sin(\Theta_i)\right] - \mathbf{G}, \quad (5)$$

where $\mathbf{G}$ is a reciprocal lattice vector. (Vectors represented by upper case letters are parallel to the surface, vectors represented by lower case letters also have a component perpendicular to the surface.) Figures 10–12 show the results for the rare gas multilayers, reduced to the first surface Brillouin zone (SBZ). Only the energy differences for features immediately to the left and right of the elastic channel which were distinct peaks in the TOF spectra are plotted. These inelastic features are fairly narrow, so it seems reasonable to attribute them to single phonon creation or annihilation. Since the observed multilayer modes disperse, multiphonon interactions should show up as very broad features. For comparison, the monolayer results are also shown. These figures show how the observed surface dynamics of these ordered adsorbate systems evolve on a layer-by-layer basis for monolayer, bilayer, and trilayer, and the comparison for thick films. The monolayer mode is dispersionless, with the adatoms behaving as independent Einstein oscillators. For the bilayer, there is a softening of the observed modes, and the adatoms no longer behave independently; the energy-momentum relationships show dispersion. For three layers, this trend is even more evident. When 20 or more layers have been deposited, the observed dispersion relations are like the surface Rayleigh wave of the bulk rare gas crystal. Within the experimental error, there is no discernable difference in the energies observed for thick films between 20 and 100 layers for the range of parallel momentum transfers we could measure. It should be noted that the phonon energies at the $\bar{M}$ point do not change much in going from bilayer to many layers, but the differences in the energies becomes increasingly more pronounced towards the center of the SBZ. This can be attributed to the proximity of the Ag substrate, as the phonon modes will involve displacements of adatoms progressively deeper into the overlayers in going from zone edge to center.[27]

There are no points presented for the thick films near the zone center. For a Rayleigh mode, ΔE goes to zero as $\mathbf{Q}$ goes to zero. For any final angle, low energy transitions are difficult to measure because the inelastic features and the elastic feature are not clearly resolvable. For the Xe trilayer, inelastic features involving small parallel momentum exchange also have fairly small values of ΔE and are merged with the elastic feature. This causes fitting problems which can result in rather large errors in determining the transition energies. For this reason, we have been more selective about the spectra plotted, and not as many points are shown here as were previously published.[28,29]

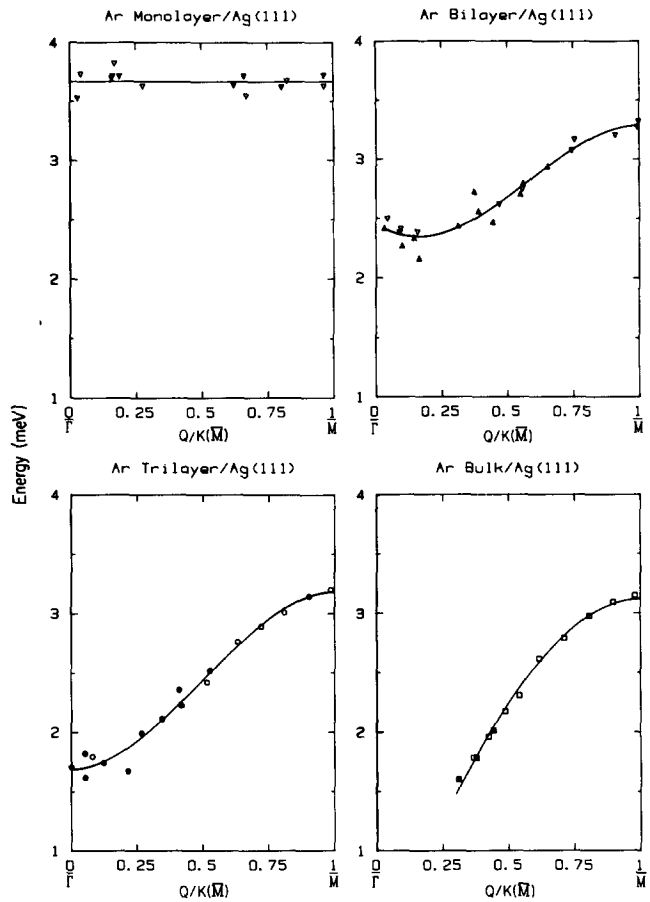

FIG. 10. The absolute values of the inelastic transition energies plotted against the absolute values of the reduced parallel momentum transfer for the Ar overlayers along the $\langle 11\bar{2}\rangle$ azimuth ($\bar{\Gamma}$–$\bar{M}$). [$K(\bar{M})$ is the position of the zone edge in reciprocal space, $2\pi/a\sqrt{3}$, where a is the lattice constant.] Open symbols are for energy loss of the scattered He (phonon creation) and closed symbols are for energy gain of the scattered He (phonon annihilation). The solid line is a cubic least-squares fit to the experimental data, with the constraints that the slope be zero at $\bar{M}$, and for the thick films, that the energy is zero at the zone center. Only the lowest energy transitions have been plotted. Bulk results are for ~30 layer films, though a few are for a 50 layer film.

Figures 13–15 are repeated zone plots for the observed inelastic transitions. In this case, points were plotted for all of the inelastic features which were distinct peaks in the TOF spectra. For the bilayers and trilayers, the solid lines are from lattice dynamics calculations of Gibson *et al.*[28] These were computed by summing the rare gas pair potentials out to fifth nearest neighbors, coupling each layer to the Ag substrate, and using the experimentally determined lattice con-

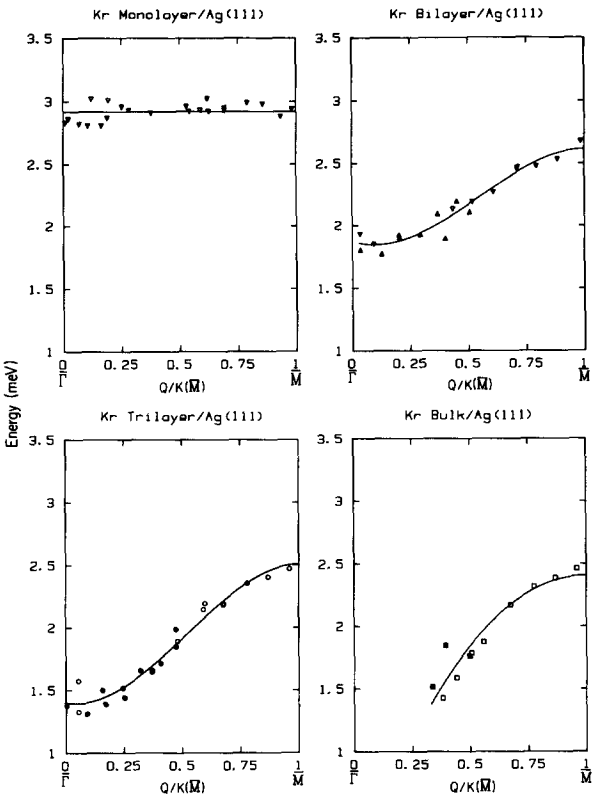

FIG. 11. The same as Fig. 10 for the Kr overlayers. Bulk results are for 28–30 layer films.

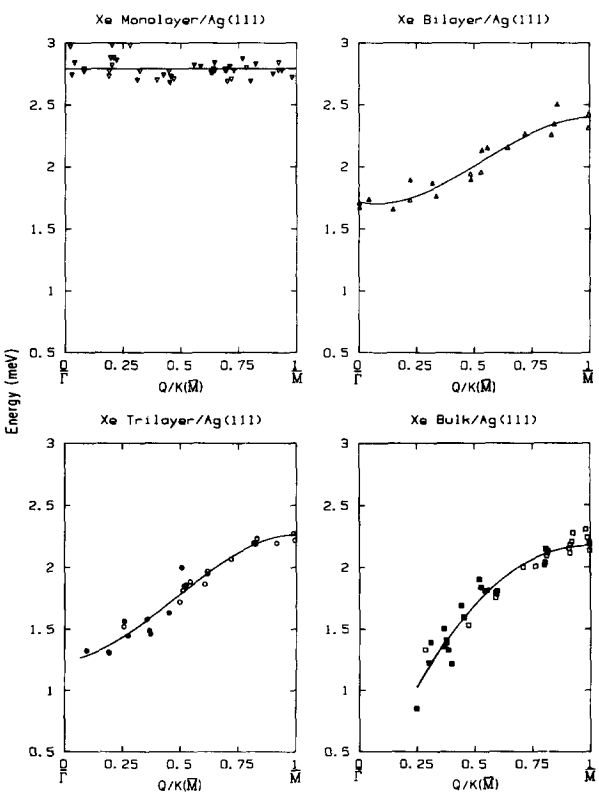

FIG. 12. The same as Fig. 10 for the Xe overlayers. Bulk results are for 20–100 layers.

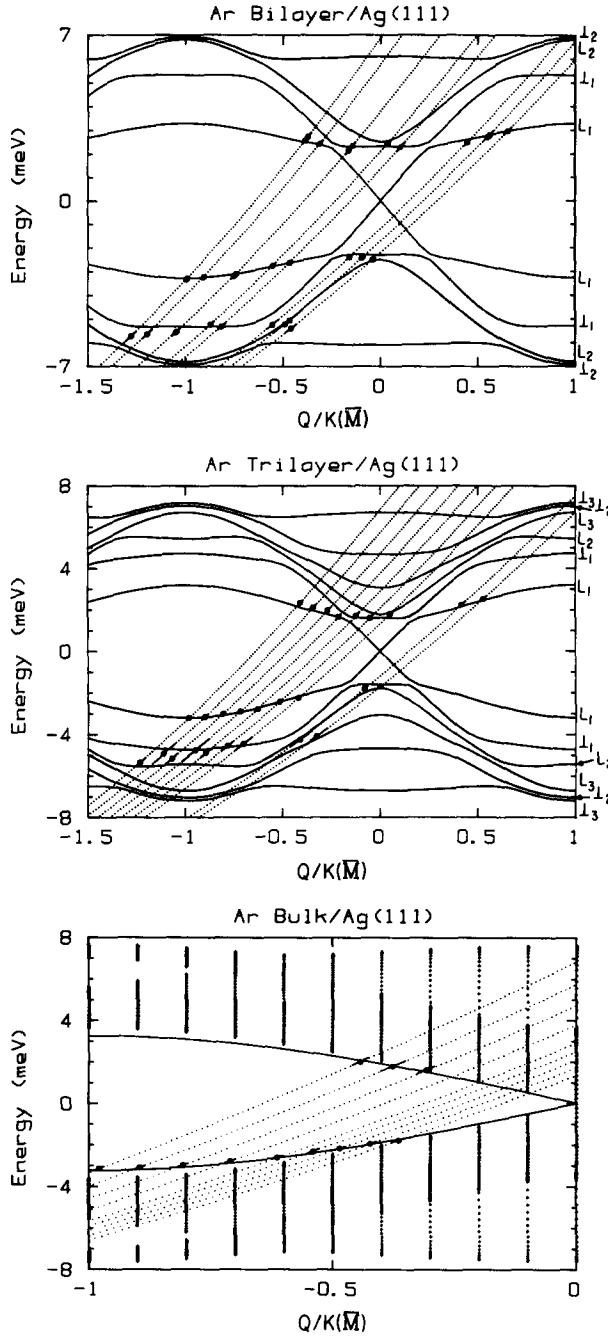

FIG. 13. Dispersion curves for the Ar multilayers in the $\bar{\Gamma}$–$\bar{M}$ direction. Experimental data and estimated error bars are plotted along with the scan curves (dotted lines). For the bilayer and trilayer, the solid lines are the calculated sagittally polarized modes from Ref. 28 (see the text). For the bulk, the solid lines are calculated values for the Rayleigh mode, and the crosses are the remainder of the modes. All of the data were taken at $\Theta_i = 45°$ with an 18 meV He beam, and the detector angles varied from 37° to 49°. From left to right, the scan curves represent increasing detector angles.

stants parallel to the surface and the bulk spacings for the interlayer distances. These calculations assumed that the Ag substrate was rigid. Since we are looking in the high symmetry direction $\bar{\Gamma}$–$\bar{M}$, the modes fall into two mutually orthogonal classes.[30] The total number of modes is $3N$, where N is the number of layers. One class, containing one-third of the modes, are shear horizontally polarized; i.e., polarized orthogonally to the sagittal plane. Since the inelastic He scat-

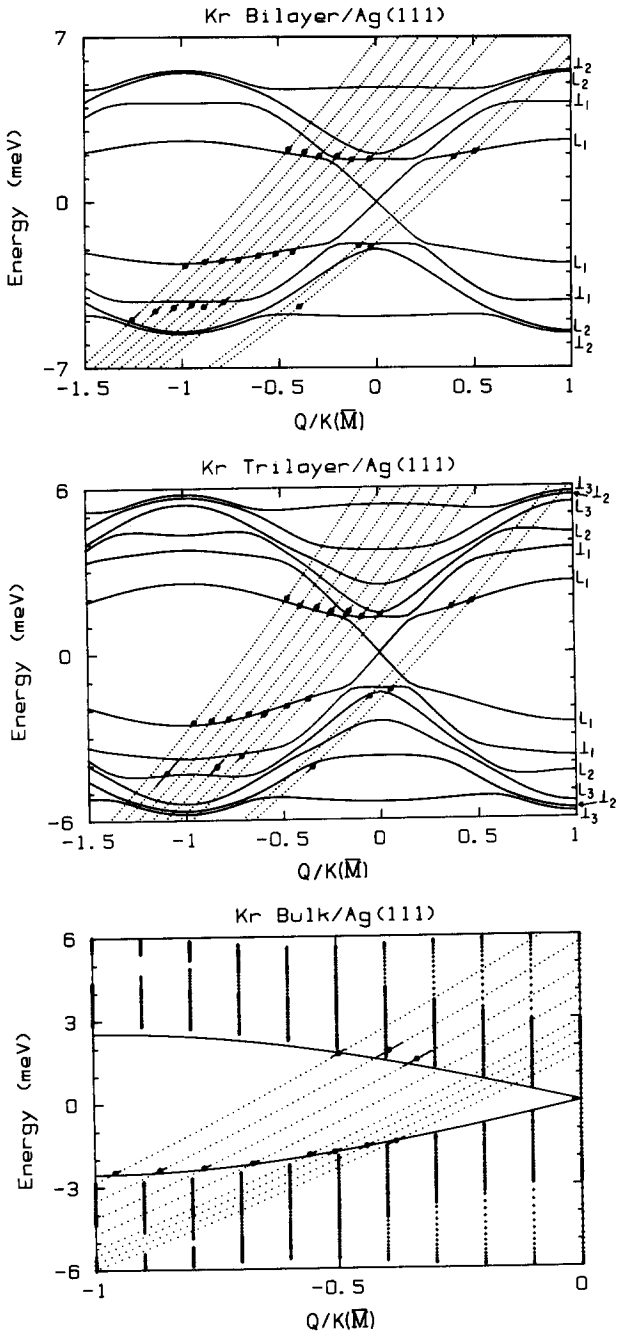

FIG. 14. The same as Fig. 13 for the Kr multilayers. All of the data were taken at $\Theta_i = 45°$ with an 18 meV He beam, and the detector angles varied from 37° to 48°. From left to right, the scan curves represent increasing detector angles.

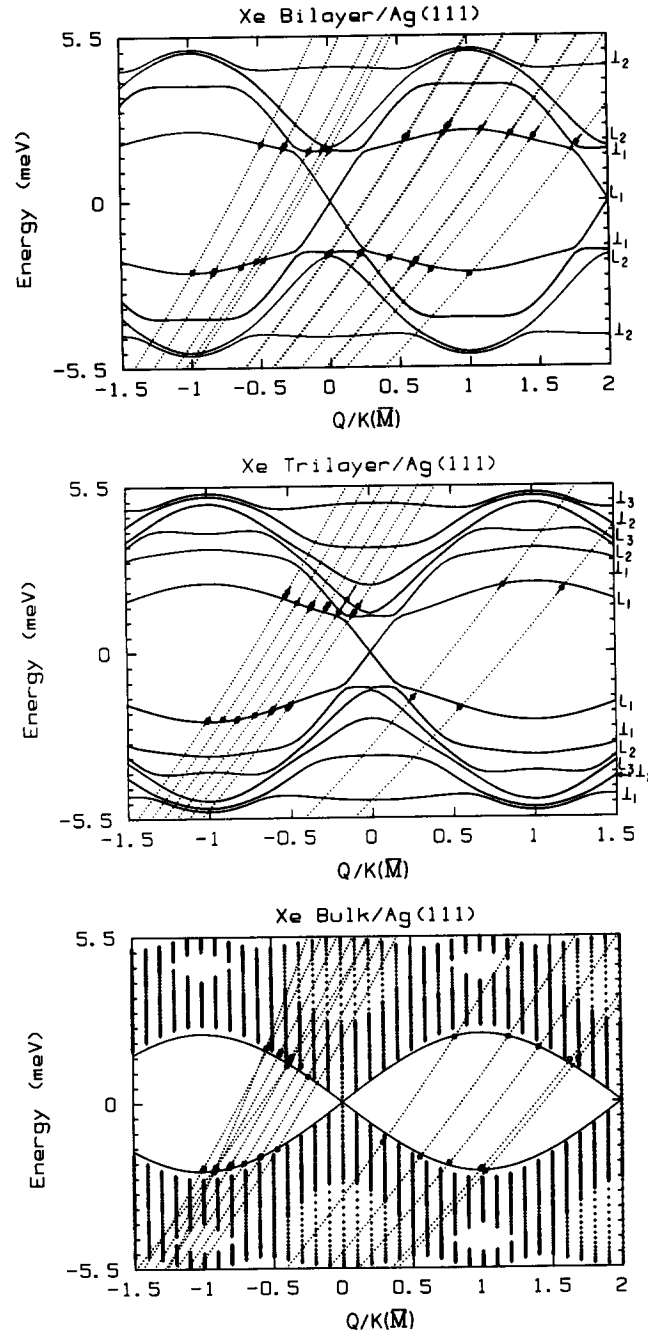

FIG. 15. The same as Fig. 13 for the Xe multilayers. For the bilayer and trilayer, all of the data were taken at $\Theta_i = 45°$ with an 18 meV He beam, and the detector angles varied from 37° to 66°. From left to right, the scan curves represent increasing detector angles. For the results labeled bulk, the data were taken with an 18 meV beam, with most of the data taken at $\Theta_i = 45°$, represented by the nearly parallel scan curves, with the detector angles varying from 37° to 66°, left to right. The scan curve with the steeper slope is for the data taken at $\Theta_i = 35°$, $\Theta_f = 28.2°$, and the scan curve with the shallowest slope is for data taken at $\Theta_i = 60°$, $\Theta_f = 51.6°$. Since the replicate data at several of the points gives an idea of the error, the error bars were not plotted.

tering intensity is most sensitive to the perpendicular displacements of the surface potential, these shear horizontal modes are not likely to contribute to the inelastic He scattering. The remainder of the modes are polarized in the sagittal plane. We observed no transitions that could be assigned to single phonon processes involving the shear horizontal modes. For this reason, only the modes that are polarized in the sagittal plane are shown. For the bulk, the calculations are for 25 layers. The solid line is the sagittally polarized surface Rayleigh wave, the other modes are represented by the small crosses. The dotted lines are the scan curves for each of the spectra, determined using the relationship

$$\mathbf{k}_i^2 \pm \frac{2nM\omega(\mathbf{Q})}{\hbar^2} - \frac{(\mathbf{K}_i + \mathbf{G} \pm \mathbf{Q})^2}{\sin^2(\Theta_f)} = 0. \qquad (6)$$

Allowed values of ΔE and $\mathbf{Q}$ fall on these lines. In the following discussion, the labeling of the modes and the values of $|e_z|^2$, the square of the eigenvector component perpendicular to the surface, are also from Ref. 28.

For the bilayers, the transitions plotted in Figs. 10–12 closely correspond to interactions with single phonons of the lowest lying sagitally polarized modes $\perp_1$ and L_1, crossing from one mode to the other for $Q/K(\bar{M})$ between 0.2–0.3. [$K(\bar{M})$ is the position of the zone edge in reciprocal space $2\pi/a\sqrt{3}$, where a is the lattice constant.] In each region, the mode observed is the one with the major proportion of $|e_z|^2$. The Xe results, for which the most data were taken, also clearly show umklapp processes. In the case of Ar and Kr, there are also distinct transitions that correspond to larger energy losses. These transitions do not in general fall on one particular mode. However, as previously pointed out,[28] these inelastic features could be due to interaction with two modes having similar values of $|e_z|^2$, and our experimental results are the unresolved combination of what are actually two peaks due to different inelastic transitions. The scan curves show that kinematically we should be able to see inelastic transitions involving phonon annhilation. In particular, $\perp_2$ has an appreciable value near $\bar{\Gamma}$, but there is no evidence of this transition in the TOF spectra. This can be at least partially understood by considering the Bose factors for phonon annihilation, $n^-(\omega)$, and phonon creation, $n^+(\omega)$, which are

$$n^-(\omega) = \left[\exp\left(\frac{\hbar\omega}{k_b T}\right) - 1\right]^{-1} \text{ and } n^+(\omega) = n^-(\omega) + 1. \tag{7}$$

Consider the interaction of the He beam with the Kr bilayer, creating or annihilating a 5 meV phonon at $T = 22$ K. Near $\bar{M}$, we see a fairly weak transition probably due to interaction with the modes $\perp_1$ and L_2 where ~ 5 meV phonons are created. The product of $|e_z^2|\cdot n^+(\omega)$, which should be proportional to the scattering intensity, will be $(0.07 + 0.04)(1.1) = 0.12$. Near $\bar{\Gamma}$, for annihilating a phonon on the $\perp_2$ mode, which has a much larger value of $|e_z^2|$, the product of $|e_z^2|\cdot n^-(\omega)$ will be only $0.26\times 0.077 = 0.02$. The ratio $n^+(\omega)/n^-(\omega)$ is about 14. In contrast, for a 2.2 meV transition at 22 K, the phonon energy for the L_1 mode at $Q/K(\bar{M}) = 0.5$, where we see both phonon creation and annihilation, the ratio of $n^+(\omega)/n^-(\omega)$ is only 3. At the temperatures of these experiments, the phonon populations for the higher energy modes weigh heavily against our seeing inelastic transitions due to phonon annihilation involving these modes.

For the Xe bilayer, only the lowest energy transitions corresponding to the $\perp_1$ and L_1 modes are observed as distinct peaks in the TOF spectra. However, as is the case for Ar and Kr, there is a broad shoulder on the low energy side of the spectra. This shoulder could be partially due to unresolved interactions with higher energy phonons. It could also be due to scattering involving multiphonon processes, which, for dispersing modes, will not show up as distinct peaks, but will be smeared over many final values of energy.

The trilayers, like the bilayers, show inelastic transitions which can be ascribed primarily to interaction with two modes, and are also plotted in Figs. 10–12. They cross from the $\perp_1$ mode to the L_1 mode in going from $\bar{\Gamma}$ to $\bar{M}$, being associated with the mode with the largest value of $|e_z^2|$. There is some discrepancy near the zone center, where the energies are slightly higher than those expected for the $\perp_1$ mode. Ar and Kr trilayers also show some distinct features at greater energy losses. These peaks could then be associated with the creation of phonons of the higher energy modes. That the energies determined for the peaks of the features in the TOF spectra do not always fall on a calculated mode may be due to the feature actually being the unresolved combination of several features resulting from interactions with more than one mode. Hybridization of the overlayer modes with those of the Ag substrate may also lead to small shifts in this region. The very broad shoulder on the right of the spectra can also be due to multiphonon interactions. As is the case with the bilayers, higher energy transitions due to phonon annihilation are not observed, being strongly disfavored by the Bose factors.

The only clearly resolved features in the TOF spectra of the thick films can be associated with the Rayleigh surface mode. There is a great deal of intensity in the low energy tails, which can be partly ascribed to processes involving the surface projection of the bulk modes, and once again, some contributions due to multiphonon processes is possible. For Xe, for which the most data were taken, umklapp processes are clearly observed.

INELASTIC SCATTERING: PROBABILITIES AND LINEWIDTHS

As was the case for the monolayers, we attempted to quantify the inelastic scattering probabilities and spectral linewidths. This was done by comparing the results of the least-squares fits of the TOF spectra with computer simulations of the instrument function. Details of this procedure are described in paper I. The determination of these quantities for the multilayers is, however, much more problematic than for the monolayers. The multilayer modes show dispersion, and the observed transitions involve smaller energy changes than was the case for the monolayers. The results of these two factors is that the features in the TOF spectra are not always well resolved. As mentioned in the previous section, the fitting function was a linear combination of Gaussian and Lorentizian line shapes, with the specific line shape used being predominately determined by the quality of the fit for each spectrum. It turns out that for many of the features, either line shape function gives an adequate fit. The positions of the maxima, and thus the experimentally determined transition energies, are not greatly affected by the choice, but the area assigned to a particular feature can vary by as much as a factor of 2. The reason for this is that the wings of the peaks are obscured when several peaks occur in close proximity, and it is here where the difference between the two line shapes is the most pronounced. Furthermore, multiphonon processes show up as broad features underneath the distinct single phonon features. However, since the linewidths of the inelastic transitions can vary as a function of parallel momentum transfer, using the area determined from the fits should give a closer value for the inelastic scattering probabilities than just using peak heights.

As can be seen from the scan curves and Figs. 7–9, the features in the spectra occur in a regular progression. From left to right, there is an energy gain feature, an elastic feature,

an energy loss feature which involves the same modes as the energy gain feature, and one or more other energy loss features. The procedure was to choose a line shape that best represented each feature over the range of angles used. To be specific, for the Ar and Kr bilayers, the elastic and lowest energy loss feature were each fit using a Gaussian line shape, while the other features were each fit with a Lorentzian line shape. For the Ar and Kr trilayers, Lorentzian line shapes were used for all of the features except for the lowest energy loss feature. In the case of the Xe multilayers, all of the features were fit using Lorentzians. This should allow us to at least make reasonable relative determinations of inelastic scattering transitions as a function of parallel momentum. Near the zone center, where the phonon energies are low, the elastic and inelastic features are merged, which may make the fits somewhat worse.

As in paper I, we also looked at the intensity of the specular scattering as a function of surface temperature and incident angle. This gives an estimate of the amount of inelastic scattering. These results were also used to derive a Debye–Waller correction for the inelastic scattering probabilities. The principal reason for including this correction here is that the Debye–Waller factor introduces angle dependent changes in the scattering probabilities that the purely kinematic simulation does not take into account. The results were fit using a simplified form for the Debye–Waller correction:

$$\frac{I_{00}}{I_0} = P_{\rm el} \exp(-\Delta k_z^2 \langle u_z^2 \rangle), \tag{8}$$

where I_{00} and I_0 are the reflected and incident intensities, respectively, $P_{\rm el}$ is the elastic intensity if the lattice were static, and Δk_z is the momentum change for the scattered He. The quantity $\langle u_z^2 \rangle$ is the mean-square displacement of the surface atoms. A more rigorous approach would be to compute a weighted average over all the modes. In light of the simple approximation we are using, it seemed reasonable to approximate $\langle u_z^2 \rangle$ using an Einstein approximation as in paper I,

$$\langle u_z^2 \rangle = \left(\frac{\hbar}{2M\omega}\right) \coth\left(\frac{\hbar\omega}{2k_b T}\right), \tag{9}$$

where k_b is Boltzmann's constant, and T is the surface temperature. The modes disperse, so we allowed ω to be a variable parameter when fitting, and the result then approximates the value for the weighted mean. The change in the perpendicular momentum was determined using

$$\Delta k_z = k_i \left(\cos^2(\Theta_i) + \frac{D}{E_i}\right)^{1/2} + k_f \left(\cos^2(\Theta_f) + \frac{D}{E_f}\right)^{1/2}, \tag{10}$$

where D is the depth of the He–surface potential. For specular scattering, incident and final values of k, E, and Θ are identical. The procedure was to use $P_{\rm el}$, ω, and D as fitting parameters, using an initial value of D estimated by summing He–rare gas pair potentials (using the HFD potential from Ref. 31), a van der Waals attraction for the He–substrate interaction,[32,33] and an estimate of the He–adatom–adatom three-body interaction for the outermost layer from Klein and Cole.[34] The derived values of D were then very close to the values of the initial guesses. All of the data for a particular overlayer were fit simultaneously, so that the results are a best least-squares fit for all of the incident angles. Figure 16 shows the experimentally determined points and the results of the fitting procedure for the Xe overlayers. The fitted lines for the Ar and Kr overlayers fit the experimental results about as well as those for Xe. Table IV gives the values of the derived values of D and $\hbar\omega$.

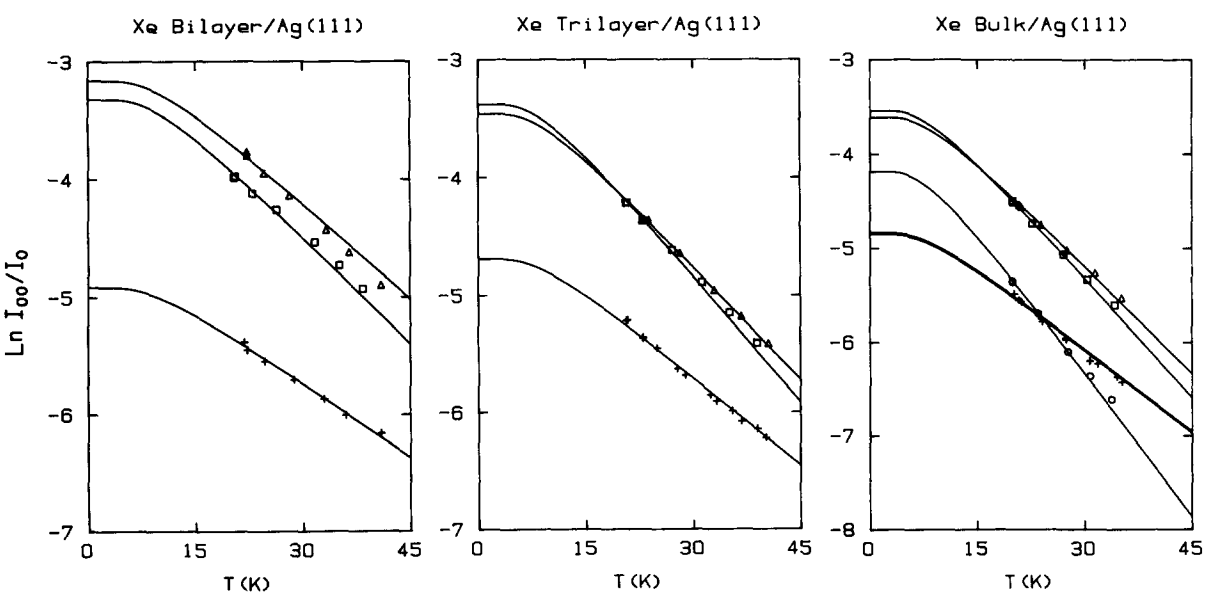

FIG. 16. The logarithm of the specular intensity divided by the incident intensity vs surface temperature for an 18 meV He beam scattering from the Xe multilayers. Solid lines are the fits (see the text). Circles are for $\Theta_i = 35°$, squares are for $\Theta_i = 45°$, triangles are for $\Theta_i = 50°$, and crosses are for $\Theta_i = 60°$. Bulk is about 25 layers. For the trilayer and bulk, the data at $\Theta_i = 60°$ are from two different overlayers. In both cases, the data sets did not have exactly the same absolute intensity, but the values of I_{00}/I_0 have been multiplied by a constant so that the data overlap.

TABLE IV. Values of Debye–Waller parameters (see the text).

	Ar $\hbar\omega$(meV)	D (meV)
Bilayer	3.25	7.42
Trilayer	2.85	7.08
Thick film	2.64	7.18
	Kr $\hbar\omega$(meV)	D (meV)
Bilayer	2.38	6.96
Trilayer	2.21	6.79
Thick film	2.13	6.85
	Xe $\hbar\omega$(meV)	D(meV)
Bilayer	2.27	6.28
Trilayer	2.07	6.08
Thick film	1.90	5.98

Figures 17–22 show the inelastic scattering probabilities, in units of probability per steradian normalized by I_{00} (i.e., $I_{\text{phonon}}/I_{00}/\text{sr}$), for the Ar and Kr multilayers. The Xe results are not plotted, since, in many instances, the structure in the probability plots is obscured by large error bars, due to the merging of the features in the TOF spectra. Some of the results for the Xe overlayers are summarized in Table V. The results have been Debye–Waller corrected to 0 K by multiplying by the factor

$$\frac{[\exp(-\Delta k_{z\,\text{ph}}^2\langle u_z^2(0)\rangle)/\exp(-\Delta k_{z\,\text{ph}}^2\langle u_z^2(T)\rangle)]}{[\exp(-\Delta k_{z\,\text{sp}}^2\langle u_z^2(0)\rangle)/\exp(-\Delta k_{z\,\text{sp}}^2\langle u_z^2(T)\rangle)]}, \tag{11}$$

where the subscripts sp and ph refer to the specular and inelastic scattering, respectively. The factors $\langle u_z^2(0)\rangle$ and $\langle u_z^2(T)\rangle$ are the mean-square displacements of the adatoms at 0 K and at the temperature of the experiment. As in the case of the monolayers, a TOF spectrum was taken on each overlayer at the same incident and detector angles. The value of $I_{\text{phonon}}/I_{00}/\text{sr}$ for the largest feature in this spectrum was then used to internormalize all of the results. We did not observe such a wide range of I_{00}/I_0 for the multilayers as for the monolayers, and so this procedure does not have much influence on the results.

One of the most notable features of the inelastic scattering probabilities is that they change by only a factor of 2 or 3 across the entire SBZ. This is in contrast to transition metal surfaces,[35–37] as well as the more corrugated Ag(001)-$c(2\times2)$Cl surface. It also appears that any falloff in inelastic scattering intensities is much less than that observed for the alkali halides.[38] Qualitatively, several reasons account for this difference. For the relatively smooth transition metal surfaces, the laterally averaged component is by far the most important part of the He–surface interaction potential. A very corrugated surface, like these rare gas overlayers, has an appreciable contribution from higher order Fourier components in the interaction potential, as shown by the elastic scattering results. This should increase the amount of inelastic scattering at positions in reciprocal space well away from the center of the first SBZ, and also allows us to see umklapp processes. In addition, although the phonon modes of the rare gas multilayers disperse, the range of energies is small compared to these other systems, with the maximum energy

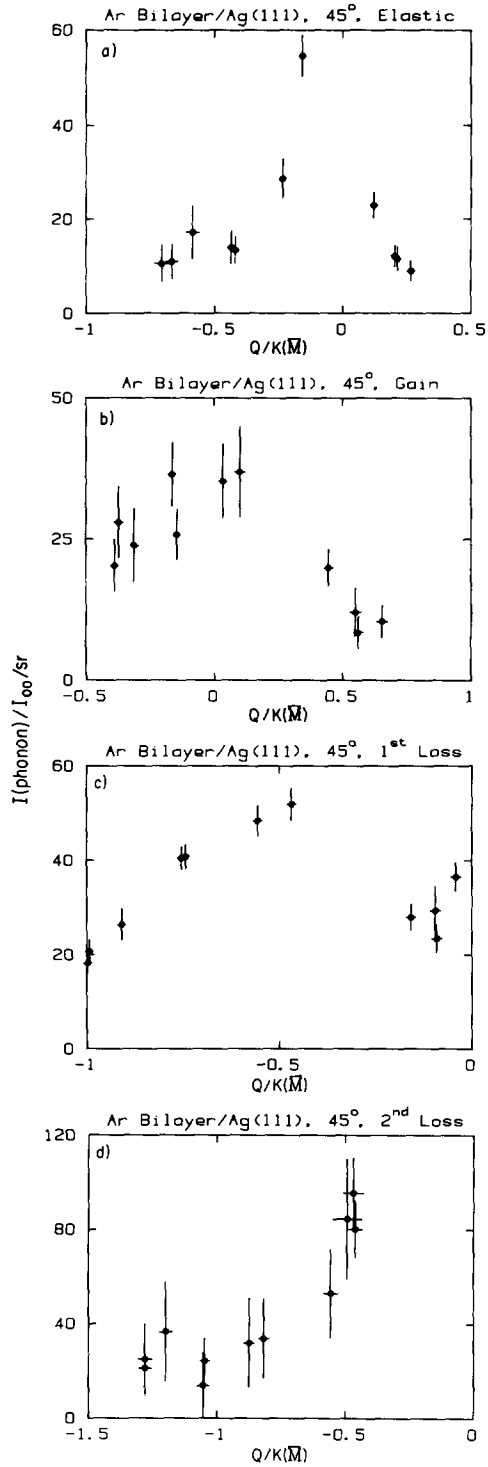

FIG. 17. Inelastic scattering probabilities for an 18 meV He beam scattering from the Ar bilayers along the $\langle 11\bar{2}\rangle$ azimuth, with $T_s = 21$ K and $\Theta_i = 45°$. Results have been Debye–Waller corrected. The label gain is for transitions where the scattered He had gained energy. The labels 1st loss and 2nd loss refer to transitions where the scattered He had lost energy, 2nd loss referring to the largest energy loss. The absolute values of the inelastic scattering probabilities are approximate, only the relative values for a particular transition are directly comparable (see the text). Debye–Waller corrected to 0 K, the average value of I_{00}/I_0 was 2.61%.

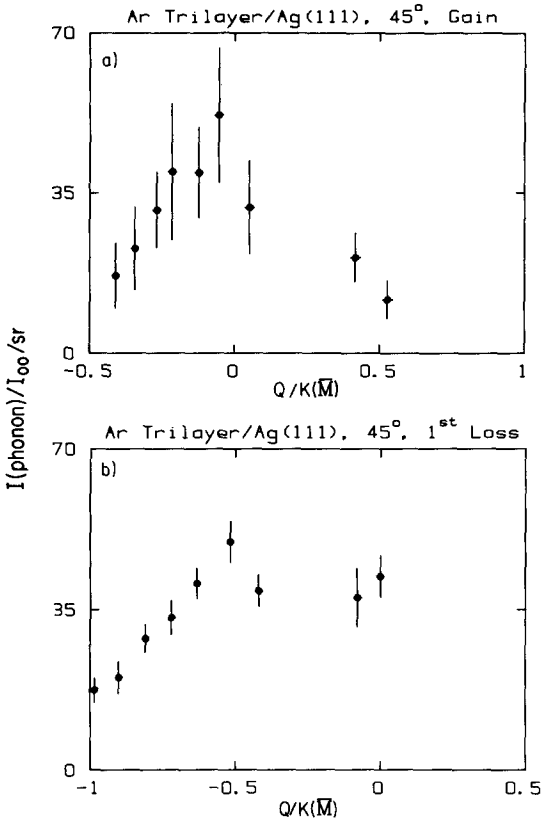

FIG. 18. The same as Fig. 17, but for the Ar trilayers. Debye–Waller corrected to 0 K, the average value of I_{00}/I_0 was 3.79%.

at $\bar{M}$ being only slightly greater than 3 meV. The differences in inelastic scattering intensities due to factors such as the change in interaction energy and bose factors are therefore much smaller for the rare gas systems.

It is worth noting that the Ar and Kr transition probability curves have qualitatively the same shape for the same transition. This similarity can be seen in the bilayer and trilayer data shown in Figs. 17, 18, 20, and 21, and persists up to the bulk limit, as shown in Figs. 19 and 22. Since there is a change in the phonon energies to larger values in going from $\bar{\Gamma}$ to $\bar{M}$, and the values of $|e_z^2|$ for the transitions plotted do

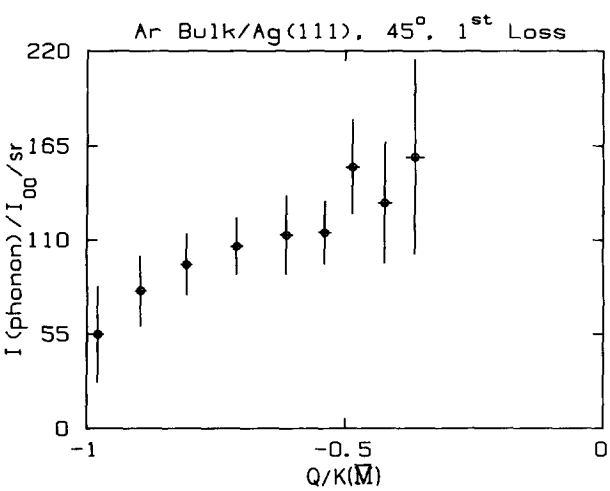

FIG. 19. The same as Fig. 17, but for 30–50 layers of Ar. Debye–Waller corrected to 0 K, the average value of I_{00}/I_0 was 2.87%.

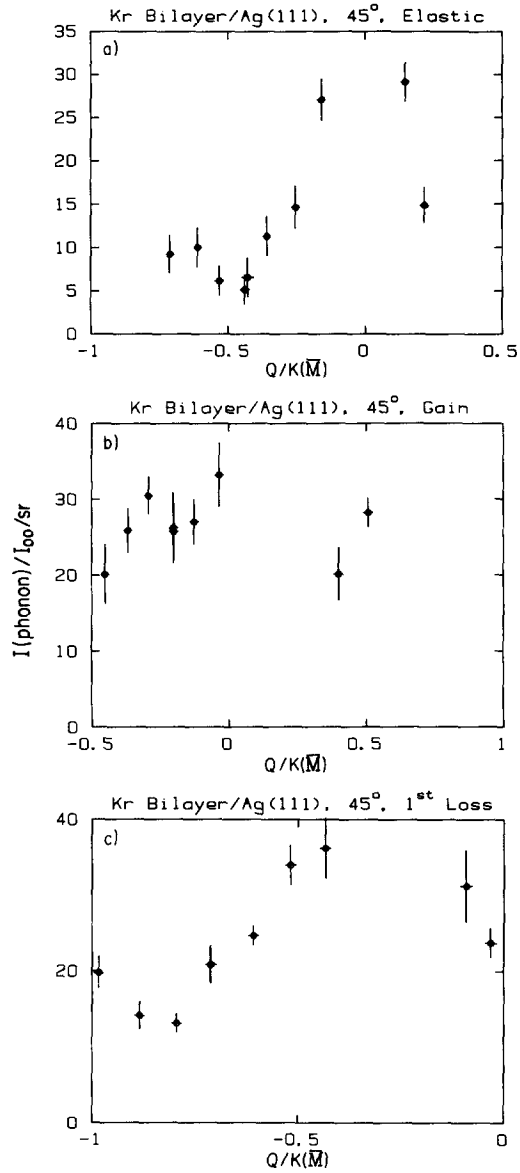

FIG. 20. The same as Fig. 17, but for the Kr bilayers, with $T_s = 22$ K. Debye–Waller corrected to 0 K, the average value of I_{00}/I_0 was 5.76%.

not change much across the SBZ, it is not surprising that there is a trend for the inelastic scattering probabilities to decrease from zone center to edge. Both the phonon annihilation and creation transitions show this trend to some extent. For the phonon creation transitions involving the Ar and Kr bilayers and trilayers, the maximum probability is away from the zone center, and slopes down in both directions of Q. The trend is most pronounced for the Ar bilayer. The maxima occur for detector angles near specular, which can introduce fitting problems, and the values near the zone center are for spectra where the inelastic feature and the elastic feature are merged (bottom spectra in Figs. 7 and 8). However, we do not feel that the results are entirely due to fitting problems. The Kr bilayer and trilayer results for phonon creation also have a minimum that is not quite at the zone edge. The Kr monolayer results also show a similar feature. Since the three overlayers have different lattice con-

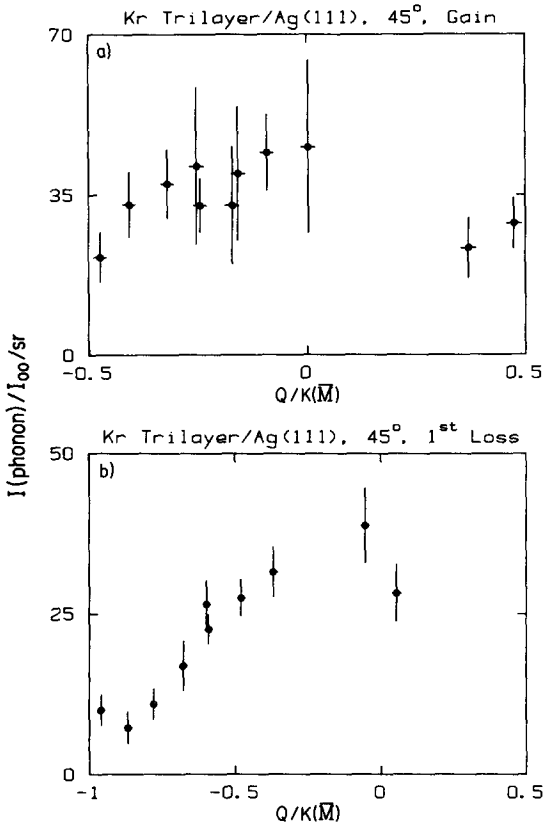

FIG. 21. The same as Fig. 17, but for the Kr trilayers, with $T_s = 22$ K. Debye–Waller corrected to 0 K, the average value of I_{00}/I_0 was 5.80%.

stants and different interaction potentials, we have no explanation for this observation.

The gain and first loss features show similar inelastic scattering probabilities. This is an artifact of the line shapes used for fitting, a Lorentzian for the gain, and a Gaussian for the first loss. If a Lorentzian is used for the loss feature also, the fits are in general not as good, but the probabilities go up by a factor of 1.6 to 1.8. This makes the ratios of gain to loss closer to the value of ~3–5 expected from the bose factors.

For scattering from the Ar bilayer, the transitions labeled second loss show an increase in the inelastic scattering

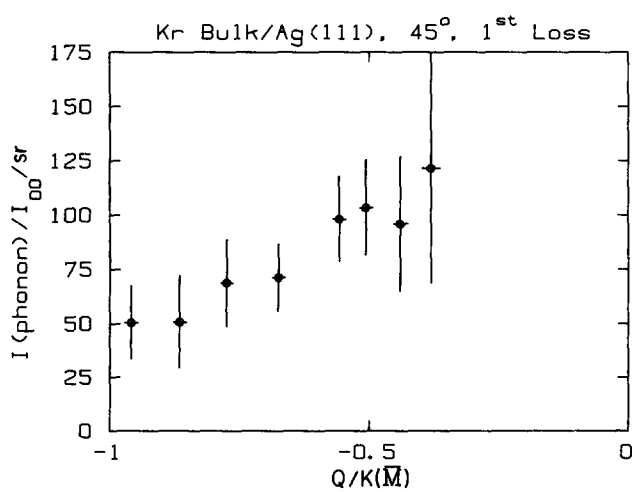

FIG. 22. The same as Fig. 17, but for 28–30 layers of Kr, with $T_s = 22$ K. Debye–Waller corrected to 0 K, the average value of I_{00}/I_0 was 3.81%.

TABLE V. Approximate average values of the I_{phonon}/I_{00}/sr and the FWHM of the energy Lorentzian used to broaden the inelastic scattering simulations for the Xe multilayers, along the $\langle 11\bar{2}\rangle$ azimuth. The surface temperature was 24 K. The values of I_{00}/I_0, Debye–Waller corrected to 0 K, are 3.38% for the bilayer, 3.72% for the trilayer, and 2.81% for the thick films. The fitting line shape was a Lorentzian in all cases, and the results are tabulated so as to give an idea of the magnitude of the inelastic scattering intensities.

	Probability (I_{phonon}/I_{00}/sr)	Width (meV)
Bilayer	30	0.5
Trilayer	30	0.5
20–27 layers	50	1

probabilities near $Q/K(\bar{M}) = 0.5$. Referring to Fig. 13, it can be seen that the two central points lie on a scan curve nearly tangent to the L_2 mode. The increase in the scattering probabilities for these points can probably be ascribed to kinematic focusing. The two outermost points do not fall on a particular mode. However, the scan curves are nearly parallel with this mode. If there is a fair amount of line shape broadening for the phonons of this mode, then the observed transition probabilities could also be largely due to kinematic focusing.

The probabilities of the elastic feature are reported only for the Ar and Kr bilayers. However, an elastic component was used in fitting all of the TOF spectra. Well away from the specular angle, this feature is most likely due to scattering from crystal defects. For the trilayers and thick films, the elastic channel is obscured by the inelastic features, and the results have large error bars. However, the probabilities do not vary by more than a factor of 2 from those seen for the monolayers. This would indicate that the defect density is not changing much as progressively more overlayers are added.

Using the procedure described in paper I, we also attempted to determine the linewidths of the transitions. The results for the transitions labeled first loss are plotted in Fig. 23. The number reported is the FWHM of the line shape that was convoluted with the instrument function and the phonon dispersion curves to reproduce the experimental widths. The transitions all show similar widths, with the bulk results being somewhat broader. One interesting feature is that the widths seem to be larger near $\bar{\Gamma}$ for the bilayers and trilayers, although the small amount of data and the fitting problems make any definite statement difficult. This may be due to enhanced coupling between the adsorbate and substrate modes in this region.[3,4,39] (The rare gas adsorbate modes overlap the substrate modes only near the center of SBZ.[3,4,39]) Within the resolution of our experiments, this would then show up as a broadening of the transitions near the zone center. The results of Kern *et al.*[9] for Kr bilayer/Pt(111) clearly show a linewidth broadening near $\bar{\Gamma}$.

Figure 24 shows the widths of the features that are labeled 2nd loss. The widths of these higher energy transitions are broader than the 1st loss transitions. This is reasonable if they correspond to experimentally unresolved interactions

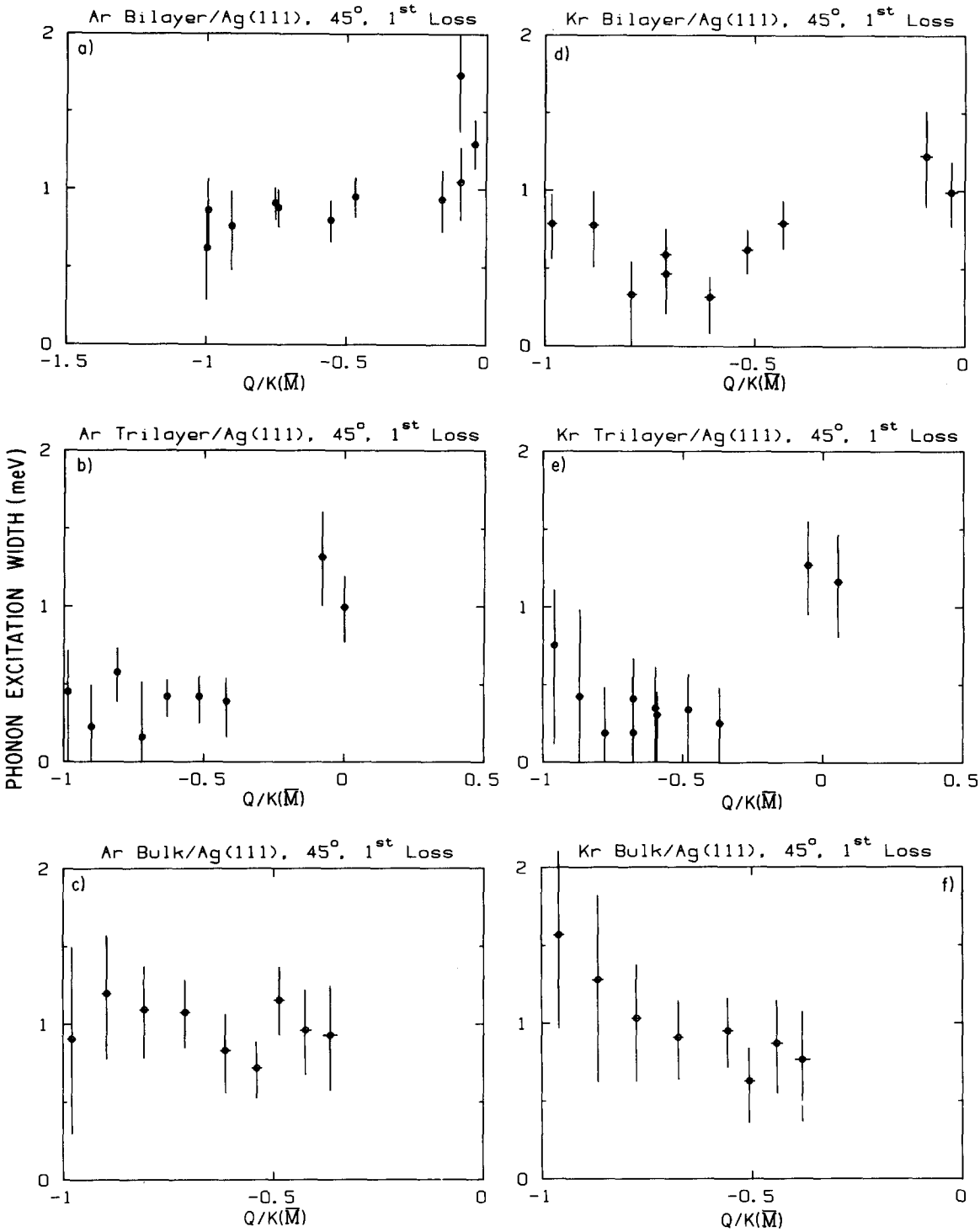

FIG. 23. The FWHM of the line shapes used to broaden the inelastic scattering simulations for the 1st loss feature of the Ar and Kr multilayers.

with more than one phonon mode. As was the case for the inelastic scattering probabilities, there is an increase in the widths for the four points near $Q/K(\bar{M}) = 0.5$. This observation is in accord with kinematic focusing. We were observing a larger section of the dispersion curve, and so a larger range of phonon energies, than was usually the case.

CONCLUSIONS

In the preceding sections, it has been rather tacitly assumed that we were observing layer by layer, or type I, growth for all of the overlayer structures. It is therefore worthwhile going over the evidence for this growth mechanism. The narrow angular widths of the observed elastic diffraction features indicate that we are not growing roughened surfaces. The thermal desorption spectra show that there are distinct desorption temperatures for each layer of rare gas, at least through three layers. One, two, and three adlayers desorb at progressively lower temperatures. Also, if a trilayer is grown, and this surface is further dosed with a small quantity of gas, a TPD spectrum shows a peak or shoulder on the

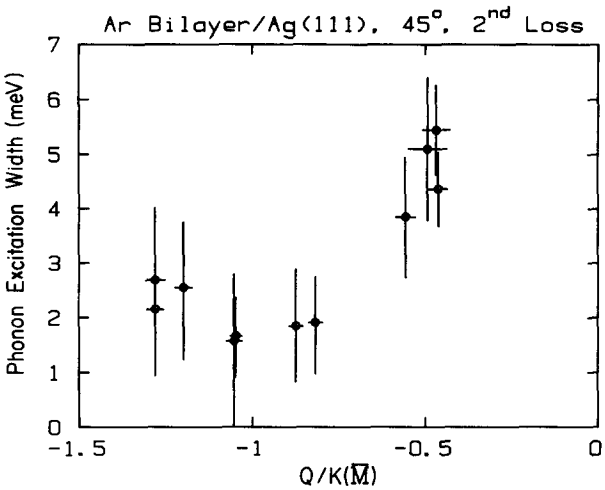

FIG. 24. The FWHM of the Lorentzian line shape used to broaden the inelastic scattering simulations for the 2nd loss feature of the Ar bilayers.

low temperature side of the trilayer peak, indicating that the third layer is more strongly bound than the fourth. This shows that adatoms in a given layer are more strongly bound than adatoms in the next layer up. Thus, for one, two, and three layers, growth should proceed on a layer-by-layer basis, as a rare gas atom will preferentially adsorb in a more strongly bound lower layer in which there are vacancies, rather than in some three-dimensional structure. The qualitative features of the isothermal desorption experiments on the Xe overlayers are consistent with type I behavior. Using low energy electron diffraction (LEED), Unguris and coworkers[12,15] measured the attenuation of a Ag diffraction peak as a function of surface temperature under a constant flux of rare gas. The LEED intensity went through two distinct steps, indicating monolayer and bilayer adsorption. This evidence indicates that the layer-by-layer growth occurs for Ar, Kr, and Xe at least for monolayer and bilayer. Further evidence for type I growth of up to four layers of Xe on Ag(111) comes from the coverage dependent Xe UPS (ultraviolet photoelectron spectroscopy) valence and XPS (x-ray photoelectron spectroscopy) core level spectra of Behm *et al.*[20] The calculations of Bruch and Ni[40] also indicate that the Xe trilayer is stable with respect to nonwettng growth. Finally, and perhaps most convincingly, there are also the distinct surface vibrational spectra for one, two, and three layers. The good fit between the experimental results and theoretical calculations (Refs. 28, 29, this paper), based upon the assumption of complete layers, would also support this conclusion. All of the evidence leads us to believe that we are seeing layer-by-layer growth on the Ag(111) substrate for Ar, Kr, and Xe.

These studies have revealed in detail how the surface dynamical properties of a thin film evolve, on a layer-by-layer basis, into those characteristic of a thick crystal. In the monolayer limit, the mode polarized normal to the surface is shown to be dispersionless, indicating that the adatoms can be treated as independent Einstein oscillators. As the film thickness is systematically increased, the vibrational energies begin to show an increasing amount of dispersion as a function of phonon wave vector. Finally, for films consisting of $\geqslant 20$ layers, a clearly developed Rayleigh wave is present—characteristic of a thick crystal. The qualitative appearance and trends present for the observed modes are the same for all three rare gases, with the principal difference being that the phonon energies for a particular value of **Q** get progressively larger going from Xe to Kr to Ar.

The rate of convergence of the surface phonon energies towards those of a thick crystal differ markedly at $\bar{\Gamma}$ and $\bar{M}$. Near $\bar{M}$, the convergence is essentially complete after only three layers, while at $\bar{\Gamma}$, large differences still exist between the trilayer results and those for the bulk Rayleigh wave. This result is not really surprising when one notes that the long wavelength excitations that occur near $\bar{\Gamma}$ penetrate deeply into the film, and are therefore sensitive to the presence of a buried interface. In contrast to this, the short wavelength excitations that occur near $\bar{M}$ are localized in the surface region, and are therefore insensitive to film thickness after a few layers are deposited. This differential sensitivity to the presence of a remote interface, as a function of wave vector, should serve as a warning to those who simply ask how many layers it takes before the surface properties of a thin film reach those of a thick crystal—the answer depends on the characteristic length scale of the property in question.

Lattice dynamics calculations using realistic potentials can quantitatively explain the phonon dispersion relations.[28,29] The bilayer and trilayer results for all three rare gases also demonstrate that the cross sections for inelastic He scattering are the largest for the modes having displacements normal to the crystal surface. This is convincingly shown in Figs. 13–15 in the region of reciprocal space where L_1 and $\perp_1$ have an avoided crossing—the scattering clearly tracks the branch having the largest value of $|e_z^2|$.

Measurements of inelastic scattering probabilities and line shapes were also presented. The accuracy of these deconvoluted values was unfortunately limited by the short flight path of our detector, which resulted in the presence of partially merged features in the experimental time-of-flight spectra. Nevertheless, the systematic trends seen within any given data set are valid. The most notable of these is that the inelastic scattering probabilities for a given phonon transition vary by no more than a factor of 2 or 3 across the entire SBZ. The observation differs from the falloff in intensity as a function of **Q** that was previously observed for transition metal surfaces.

ACKNOWLEDGMENTS

We would like to thank C. F. Yu and D. Padowitz for experimental assistance, and Burl M. Hall, D. L. Mills, and J. E. Black for theoretical collaboration. We also thank M. B. Webb, L. W. Bruch, and M. L. Klein for valuable discussions. This work was supported, in part, by the U. S. Office of Naval Research and the National Science Foundation Materials Research Laboratory at the University of Chicago, DMR-8519460. S. J. S. also acknowledges support from a Camille and Henry Dreyfus Young Faculty Grant, and an I. B. M. Faculty Development Award.

[1]K. D. Gibson and S. J. Sibener, J. Chem. Phys. **88**, 7862 (1988).
[2]K. D. Gibson and S. J. Sibener, J. Vac. Sci. Technol. A **3**, 1453 (1985).
[3]K. D. Gibson and S. J. Sibener, Phys. Rev. Lett. **55**, 1514 (1985).
[4]K. D. Gibson and S. J. Sibener, Faraday Discuss. Chem. Soc. **80**, 203 (1985).
[5]B. F. Mason and B. R. Williams, Surf. Sci. **111**, 609 (1981).
[6]B. F. Mason and B. R. Williams, Phys. Rev. Lett. **46**, 1138 (1981).
[7]B. F. Mason and B. R. Williams, Surf. Sci. **139**, 173 (1984).
[8]K. Kern, R. David, R. L. Palmer, and G. Comsa, Phys. Rev. Lett. **56**, 2823 (1986).
[9]K. Kern, P. Zeppenfeld, R. David, and G. Comsa, Phys. Rev. B **35**, 886 (1987).
[10]P. I. Cohen, J. Unguris, and M. B. Webb, Surf. Sci. **58**, 429 (1976).
[11]L. W. Bruch, P. I. Cohen, and M. B. Webb, Surf. Sci. **59**, 1 (1976).
[12]J. Unguris, L. W. Bruch, E. R. Moog, and M. B. Webb, Surf. Sci. **87**, 415 (1979).
[13]L. W. Bruch, J. Unguris, and M. B. Webb, Surf. Sci. **87**, 437 (1979).
[14]L. W. Bruch and J. M. Phillips, Surf. Sci. **91**, 1 (1980).
[15]J. Unguris, L. W. Bruch, E. R. Moog, and M. B. Webb, Surf. Sci. **109**, 522 (1981).
[16]J. Unguris, L. W. Bruch, M. B. Webb, and J. M. Phillips, Surf. Sci. **114**, 219 (1982).
[17]C. A. Becker, Ph. D. thesis, University of Chicago, 1980.
[18]K. D. Gibson, C. Cerjan, J. C. Light, and S. J. Sibener, J. Chem. Phys. **88**, 7911 (1988).
[19]P. Korpiun and E. Lüscher, in *Rare Gas Solids*, edited by M. L. Klein and J. A. Venables (Academic, London, 1977), Vol. 2, Chap. 12.
[20]R. J. Behm, C. R. Brundle, and K. Wandelt, J. Chem. Phys. **85**, 1061 (1986).
[21]R. Opila and R. Gomer, Surf. Sci. **112**, 1 (1981).
[22]P. J. Estrup, E. F. Greene, M. J. Cardillo, and J. C. Tully (to be published).
[23]J. A. Venables and M. Bienfait, Surf. Sci. **61**, 667 (1976).
[24]R. K. Crawford, in *Rare Gas Solids*, edited by M. L. Klein and J. A. Venables (Academic, London, 1977), Vol. 2, Chap. 11.
[25]S. Efrima, K. F. Freed, C. Jedrzejek, and H. Metiu, Chem. Phys. Lett. **74**, 43 (1980).
[26]J. C. Tully, Surf. Sci. **111**, 461 (1981).
[27]H. Ibach and D. L. Mills, *Electron Energy Loss Spectroscopy and Surface Vibrations* (Academic, New York, 1982).
[28]K. D. Gibson, S. J. Sibener, B. M. Hall, D. L. Mills, and J. E. Black, J. Chem. Phys. **83**, 4256 (1985).
[29]G. G. Cardini, S. F. O'Shea, M. Marchese, and M. L. Klein, Phys. Rev. B **32**, 4261 (1985); G. Cardini, S. F. O'Shea, and M. L. Klein, Faraday Discuss. Chem. Soc. **80**, 227 (1985).
[30]R. E. Allen, G. P. Alldredge, and F. W. de Wette, Phys. Rev. B **4**, 1661 (1971).
[31]K. M. Smith, A. M. Rulis, G. Scoles, R. A. Aziz, and V. Nain, J. Chem. Phys. **67**, 152 (1977).
[32]E. Zaremba and W. Kohn, Phys. Rev. B **13**, 2270 (1976).
[33]L. W. Bruch, Surf. Sci. **125**, 194 (1983).
[34]J. R. Klein and M. W. Cole, Surf. Sci. **134**, 722 (1983).
[35]V. Celli, G. Benedek, U. Harten, J. P. Toennies, R. B. Doak, and V. Bortolani, Surf. Sci. **143**, L376 (1984).
[36]W. R. Lambert, M. J. Cardillo, P. L. Trevor, and R. B. Doak, Surf. Sci. **145**, 519 (1984).
[37]D. Eichenauer, U. Harten, J. P. Toennies, and V. Celli, J. Chem. Phys. **86**, 3693 (1987).
[38]R. B. Doak, Ph. D. dissertation, MIT, 1981.
[39]B. Hall, D. L. Mills, and J. E. Black, Phys. Rev. B **32**, 4932 (1985).
[40]L. W. Bruch and X.-C. Ni, Faraday Discuss. Chem. Soc. **80**, 217 (1985).